# Ocean wave parameters and spectrum estimated from single and dual high-frequency radar systems

# Ocean wave parameters and spectrum estimated from single and dual high-frequency radar systems

**Yukiharu Hisaki**

**Abstract** The high-frequency (HF) radar inversion algorithm for spectrum estimation (HIAS) can estimate ocean wave directional spectra from both dual and single radar. Wave data from a dual radar and two single radars are compared with in-situ observations. The agreement of the wave parameters estimated from the dual radar with those from in-situ observations is the best of the three. In contrast, the agreement of the wave parameters estimated from the single radar in which no Doppler spectra are observed in the cell closest to the in-situ observation point is the worst among the three. Wave data from the dual radar and the two single radars are compared. The comparison of the wave heights estimated from the single and dual radars shows that the area sampled by the Doppler spectra for the single radar is more critical than the number of Doppler spectra in terms of agreement with the dual-radar-estimated wave heights. In contrast, the comparison of the wave periods demonstrates that the number of Doppler spectra observed by the single radar is more critical for agreement of the wave periods than the area of the Doppler spectra. There is a bias directed to the radar position in the single radar estimated wave direction.

## 1 Introduction

A high-frequency (HF) ocean radar can estimate the surface currents and ocean wave spectra from the Doppler spectra, which are obtained by analyzing

Y. Hisaki
Aza-Senbaru 1, Nishihara-cho, Nakagami-gun, Okinawa, Japan
Tel.: +81-98-8515
Fax: +81-98-8552
E-mail: hisaki@sci.u-ryukyu.ac.jp

the backscattered signals of HF radio waves from the sea surface. The wave spectrum can be estimated from the Doppler spectrum on the basis of the relationship between the Doppler spectrum and the ocean wave spectrum (e.g., Barrick, 1971; Barrick and Weber, 1977; Gill and Walsh, 2001; Gill et al., 2006; Hisaki, 1999; Hisaki and Tokuda, 2001).

More than two radars are deployed to measure the surface current vectors in the east of Okinawa Island (Figure 1) (e.g., Hisaki et al.,2001) , west of Okinawa Island (Hisaki and Imadu, 2009), and Yaeyama Islands (Hisaki et al., 2016), which is located in the south of the East China Sea. Most of the methods to estimate the ocean wave directional spectrum from the HF radar require dual radar systems (Wyatt, 1991; Howell and Walsh, 1993; Hisaki, 1996; Hashimoto and Tokuda, 1999), and the wave spectrum is estimated at the intersection point of the radar beams. The signal-to-noise (SN) ratio of both Doppler spectra from both radars must be high in order to estimate the wave spectrum. However, there may be cases where only a single radar can be operated or deployed; thus, it is useful to develop a method for a single radar array.

Hisaki (1996) described a method for discretizing the integral equation which describes the relationship between the Doppler spectrum and the ocean wave spectrum. Hisaki (2005, 2006, 2009, 2014) described a method for incorporating the energy balance equation and regularization in the case of the single radar. In this method, the wave spectra are estimated on radial grids with the origin at the radar position. Only one other study has estimated the wave directional spectra from single HF radar using inversion (de Valk et al., 1999). Gurgel et al. (2006) also estimated the wave spectra from single radar using the empirical method.

Hisaki (2015) developed a method to estimate the ocean wave spectra, which can be applied to multiple, dual, and single radar cases. The method is named HF radar inversion algorithm for spectrum estimation (HIAS). The wave spectra are estimated at regular grids in the HIAS. The method to select the Doppler spectra using a self-organization map analysis (Hisaki 2013) is also described in Hisaki (2015). The method, which can be applied to both dual and single radar, is useful, because even if one of the radars is stopped during the operation of the dual radar system, the wave data can be obtained continuously. However, the wave estimation from the single radar was not demonstrated in Hisaki (2015).

To date, there have been no comparisons of the wave data estimated from the single and from dual radar systems. The objective of the present study is to compare the radar-estimated wave spectra from the single and dual radar arrays.

The outline of the method is described in Section 2.1. Sections 2.2 and 2.3 describe the discretization. The wave parameters for the comparison are summarized in Section 2.4. The number of the Doppler spectra, which is important for the comparison is presented in Section 3.1. Examples of the directional spectrum comparison are provided in Section 3.2. The comparison of the wave parameters with in-situ observations is described in Section 3.3.

The comparisons of the wave parameters from the dual and single radar are presented in Sections 3.4 and 3.5. Section 4 contains a discussion of the results, and Section 5 summarizes the conclusions and addresses the next subjects.

## 2 Method

### 2.1 Outline of the method

The method of estimating the ocean wave spectra was described in Hisaki (1996, 2005, 2006, 2009, 2014, 2015). Herein, we describe the method in detail only the points that were omitted from the previous studies. The outline of the method is briefly presented.

The constraints between the ocean wave spectra and the Doppler spectra are as follows: (c1) the relationship between the first-order scattering and the ocean wave spectrum, (c2) the relationship between the second-order scattering and the ocean wave spectrum, (c3) the energy balance equation, (c4) the two-dimensional continuity equation of the wind, (c5) the smooth spectral values in the frequency-direction plane, and (c6) a small propagation term in the energy balance equation. Constraint (c5) acts as the regularization constraint in the frequency-direction plane, and constraint (c6) acts as the regularization constraint in the horizontal plane. The solution to minimize the weighted squared sum of these constraints is estimated, and the wave spectra are estimated. The weights of constraints (c1) and (c2) are proportional to the number of the Doppler spectra for the wave estimation (Hisaki, 2015).

The first step for the nonlinear minimization problem is the Monte Carlo method. The wave spectra are the same in the wave estimation area, and the spectra are expressed using the parametric form. The parameters are estimated by generating random values for the decided ranges of the parameters. The objective function from (c1) and (c2) is evaluated for the parameters, and the parameters to minimize the objective function are obtained.

The second step is to obtain the wave spectra to minimize the objective function from (c1), (c2), and (c4). The wave spectra are also the same in the wave estimation area, but the spectra are not expressed by the parametric form but instead by the values at the discretized wave frequencies and directions.

The final step is to obtain the wave spectra to minimize the objective function from (c1) to (c6). The method is described in Hisaki (2006). If the iteration in the final step does not converge adequately, the initial guess in the the first step is changed by selecting another "seed" from which to generate random numbers.

The parameters are normalized in terms of the Bragg frequency $f_B$, the radian Bragg frequency $\omega_B = 2\pi f_B$ and the Bragg wave number $2k_0$, where $k_0$ is the radio wave number. The rightmost lower subscript 'N' denotes the normalized values.

The unknowns are the ocean wave spectral values, the wind directions ($\theta_w$), and the normalized wind speeds ($u_{wN}$) by the Bragg wave speed ($\omega_B/(2k_0)$).

The derivatives of the constraints (c1) to (c6) with respect to the unknowns are calculated to solve the nonlinear minimization problem. The derivatives of the source function with respect to ocean wave spectra, $\theta_w$ and $u_{wN}$ are calculated for the nonlinear minimization problem.

## 2.2 Discretization of the wave spectrum

A wave spectrum at arbitrary wave frequency ($\omega_N$), wave direction ($\theta$), and position ($x_N, y_N$) is expressed in terms of wave spectra at the wave frequency, wave direction, horizontal space ( $\omega_N - \theta - x_N - y_N$ ) grid points. A wave spectrum $G_N(\omega_N, \theta) = G_N(\omega_N, \theta, x_N, y_N)$ is expressed as

$$G_N(\omega_N, \theta) = \sum_{n_1=1}^{2} \sum_{n_2=1}^{2} w(n_1, n_2) G_N(\tilde{\omega}_N(k_f + n_1 - 1), \tilde{\theta}(l_d + n_2 - 1)), \quad (1)$$

where

$$w(n_1, n_2) = w_\omega(n_1) w_d(n_2), \quad (2)$$

$$w_\omega(n_1) = w_d(n_2) = 0 \quad \text{for} \quad \omega_N < \omega_{minN}, \quad (3)$$

$$w_\omega(1) = \frac{\log(\omega_{minN}) + \log(\Delta_\omega) k_f - \log(\omega_N)}{\log(\Delta_\omega)}$$

$$\text{for} \quad \omega_{minN} \leq \omega_N \leq \omega_{maxN}, \quad (4)$$

$$w_\omega(2) = 1 - w_\omega(1) \quad \text{for} \quad \omega_{minN} \leq \omega_N \leq \omega_{maxN}, \quad (5)$$

$$w_\omega(1) = (\omega_N^{-1} \omega_{maxN})^p \quad \text{for} \quad \omega_N > \omega_{maxN}, \quad (6)$$

$$w_\omega(2) = 0 \quad \text{for} \quad \omega_N > \omega_{maxN}, \quad (7)$$

$$w_d(1) = \frac{-\pi + \Delta_\theta l_d - \theta}{\Delta_\theta}, \quad (8)$$

$$w_d(2) = 1 - w_d(1), \quad (9)$$

and $\tilde{\omega}_N(k_f) = \omega_{minN} \Delta_\omega^{k_f - 1}$, $\tilde{\theta}(l_d) = -\pi + \Delta_\theta(l_d - 1)$, and $\omega_{maxN} = \tilde{\omega}_N(M_f)$. Here, $\Delta_\omega$ is the frequency resolution, $\Delta_\theta$ is the direction resolution, $M_f$ is the number of wave frequencies, $\omega_{minN}$ is the minimum wave frequency and $p = 4$. The wave frequency and direction index number $k_f$ and $l_d$ in Eq. (1) are determined to satisfy the relations

$$\frac{\log(\omega_N/\omega_{minN})}{\log(\Delta_\omega)} \leq k_f < 1 + \frac{\log(\omega_N/\omega_{minN})}{\log(\Delta_\omega)} \quad \text{for} \quad \omega_{minN} \leq \omega_N \leq \omega_{maxN}, \quad (10)$$

$$k_f = M_f, \quad \text{for} \quad \omega_N > \omega_{maxN}, \quad (11)$$

and

$$\frac{\theta + \pi}{\Delta_\theta} \leq l_d < 1 + \frac{\theta + \pi}{\Delta_\theta}. \quad (12)$$

The parameters for the discretization such as $\Delta_\omega$, $\Delta_\theta$, $\omega_{minN}$ and $M_f$ are the same as those in Hisaki (2015).

## 2.3 Discretization of the energy balance equation

We did not use numerical differentiation to evaluate the derivatives of constraints (c1) to (c6). These derivatives are written analytically and are calculated. For example, the derivatives with respect to the unknowns of the source function in the energy balance equation are evaluated. The derivatives of the wind input and the dissipation source functions can be written analytically. The derivatives of the propagation term can also be written analytically from equation (15) in Hisaki (2015).

The nonlinear interaction source function in the energy balance equation uses the Discrete Interaction Approximation (DIA). The nonlinear interaction is represented by the discrete interactions for a single representative quadruplet $(\omega_i, \theta_i)$ $(i = 1, 2, 3, 4)$, where $(\omega_i, \theta_i)$ is the radian wave frequency and direction of the quadruplet.

The increment of the nonlinear interaction source function is written using equation (5.5) of Hasselmann et al. (1985) as

$$\begin{pmatrix} \delta S_{NlN} \\ \delta S_{NlN}^+ \\ \delta S_{NlN}^- \end{pmatrix} = \begin{pmatrix} -2 \\ 1 \\ 1 \end{pmatrix} D_N(\omega_{1N}, \omega_{3N}, \omega_{4N}, \theta, \theta_3, \theta_4), \quad (13)$$

$$D_N(\omega_{1N}, \omega_{3N}, \omega_{4N}, \theta, \theta_3, \theta_4) = (2\pi)^{-9} C_0 \omega_{1N}^{11} \Big[ (G_N(\omega_{1N}, \theta))^2 \Big\{ \frac{G_N(\omega_{3N}, \theta_3)}{(1 + \lambda_{Nl})^4} $$
$$+ \frac{G_N(\omega_{4N}, \theta_4)}{(1 - \lambda_{Nl})^4} \Big\} $$
$$- 2\frac{G_N(\omega_{1N}, \theta) G_N(\omega_{3N}, \theta_3) G_N(\omega_{4N}, \theta_4)}{(1 - \lambda_{Nl}^2)^4} \Big] (14)$$

where $\delta S_{NlN}$, $\delta S_{NlN}^+$ and $\delta S_{NlN}^-$ are increments at wave vectors $\mathbf{k}_{1N}(= \mathbf{k}_{2N})$, $\mathbf{k}_{3N}$ and $\mathbf{k}_{4N}$ respectively, $\lambda_{Nl} = 0.25$ and $C_0 = 3 \times 10^7$. The resonance conditions

$$\mathbf{k}_{1N} + \mathbf{k}_{2N} = \mathbf{k}_{3N} + \mathbf{k}_{4N}, \quad (15)$$

$$\omega_{1N} + \omega_{2N} = \omega_{3N} + \omega_{4N} \quad (16)$$

are satisfied, and $(\omega_{3N}, \omega_{4N}) = (1 + \lambda_{Nl}, 1 - \lambda_{Nl})\omega_{1N}$ (e.g., Hasselmann et al., 1985).

Equation (13) is written in terms of the source function to calculate the derivative of the nonlinear source function analytically. If $(\omega_{1N}, \theta_1) = (\omega_{2N}, \theta_2)$ is on the frequency-direction $(\omega_N - \theta)$ discretized grid point, then $(\omega_{3N}, \theta_3)$ and $(\omega_{3N}, \theta_3)$ are not on the $\omega_N - \theta$ discretized grid point. If $(\omega_{3N}, \theta_3)$ (or $(\omega_{4N}, \theta_4)$) is on the frequency-direction $(\omega_N - \theta)$ discretized grid point, $(\omega_{1N}, \theta_1)$ and $(\omega_{4N}, \theta_4)$ (or $(\omega_{3N}, \theta_3)$) are not on the $\omega_N - \theta$ discretized grid point.

Therefore, we classified into three cases for calculation of the nonlinear interaction term $(\omega_N, \theta) = (\omega_{1N}, \theta_1) = (\omega_{2N}, \theta_2)$, $(\omega_N, \theta) = (\omega_{3N}, \theta_2)$, and $(\omega_N, \theta) = (\omega_{4N}, \theta_3)$. In the case of $(\omega_N, \theta) = (\omega_{1N}, \theta_1) = (\omega_{2N}, \theta_2)$, the increment $\delta S_{NlN}/2$ in Eq. (13) is evaluated. In the cases of $(\omega_N, \theta) = (\omega_{3N}, \theta_3)$

and $(\omega_N, \theta) = (\omega_{4N}, \theta_4)$ the increments $\delta^+ S_{NlN}$ and $\delta^- S_{NlN}$ in Eq. (13) are evaluated, respectively.

These calculations are summarized into the following equation, and the normalized nonlinear interaction term $S_{NlN}$ is written in terms of the discretized form as

$$S_{NlN}(\omega_N, \theta) = \sum_{i=1}^{4} \sum_{n=1}^{2} (-1)^{\text{int}((i+1)/2)} D_N(\omega_{1N}^{(i)}, \omega_{3N}^{(i)}, \omega_{4N}^{(i)}, \theta_1(n)^{(i)}, \theta_3(n)^{(i)}, \theta_4(n)^{(i)}),$$
(17)

where $\text{int}(a)$ denotes the integer part of $a$,

$$\omega_{1N}^{(i)} = \omega_N \quad (\text{for} \quad i = 1, 2), \tag{18}$$
$$\omega_{1N}^{(3)} = (1 + \lambda_{Nl})^{-1} \omega_N, \tag{19}$$
$$\omega_{1N}^{(4)} = (1 - \lambda_{Nl})^{-1} \omega_N, \tag{20}$$
$$\omega_{3N}^{(i)} = (1 + \lambda_{Nl}) \omega_{1N}^{(i)} \quad (\text{for} \quad i = 1, 2, 3, 4), \tag{21}$$
$$\omega_{4N}^{(i)} = (1 - \lambda_{Nl}) \omega_{1N}^{(i)} \quad (\text{for} \quad i = 1, 2, 3, 4), \tag{22}$$
$$\theta_1(n)^{(i)} = \theta \quad (\text{for} \quad i = 1, 2, \quad \text{and} \quad n = 1, 2), \tag{23}$$
$$\theta_1(n)^{(3)} = \theta + (2n - 3)\theta_+ \quad (\text{for} \quad n = 1, 2), \tag{24}$$
$$\theta_1(n)^{(4)} = \theta + (3 - 2n)\theta_- \quad (\text{for} \quad n = 1, 2), \tag{25}$$
$$\theta_3(n)^{(i)} = \theta_1(n)^{(i)} + (3 - 2n)\theta_+ \quad (\text{for} \quad i = 1, 2, 3, 4, \quad \text{and} \quad n = 1, 2), \tag{26}$$
$$\theta_4(n)^{(i)} = \theta_1(n)^{(i)} + (2n - 3)\theta_- \quad (\text{for} \quad i = 1, 2, 3, 4, \quad \text{and} \quad n = 1, 2), \tag{27}$$

and $\theta_+ = 11.5°$, $\theta_- = 33.6°$, which is derived from the resonance conditions (Eqs. (15) and (16)) and $(\omega_{3N}, \omega_{4N}) = (1 + \lambda_{Nl}, 1 - \lambda_{Nl})\omega_{1N}$ (e.g., Hasselmann et al., 1985). The index number $i$ in Eq. (27) denotes that $\omega_N$ in Eq. (27) corresponds to $\omega$ of Equation (5.1) in Hasselmann et al. (1985) for $i = 1$ and $i = 2$; $\omega_N$ in Eq. (27) corresponds to $\omega_+$ in Equation (5.2) of Hasselmann et al. (1985) for $i = 3$, and $\omega_N$ in Eq. (27) corresponds to $\omega_-$ in Equation (5.3) of Hasselmann et al. (1985) for $i = 4$. The index number $n = 2$ in Eq. (27) corresponds to the mirror image of the first quadruplet $n = 1$ with relative angles of $\theta_+$ and $-\theta_-$. The function $D_N$ in Eq. (27) is calculated from $G_N$ as

$$G_N(\omega_{mN}^{(i)}, \theta_m(n)^{(i)}) = \sum_{n_1=1}^{2} \sum_{n_2=1}^{2} w_{Nl} G_N(k_\omega + n_1 - 1, l_\theta + n_2 - 1), \quad m = 1, \ldots, 4$$
(28)

where $k_\omega = k_\omega(k_f, m, i, n, n_1, n_2)$ is the frequency number, $l_\theta = l_\theta(l_d, m, i, n, n_1, n_2)$ is the direction number which satisfies relations (10), (11), and (12), and $G_N(k_\omega, l_\theta) = G_N(\tilde{\omega}_N(k_\omega), \tilde{\theta}(l_\theta))$. The weight $w_{Nl} = w_{Nl}(k_f, l_d, m, i, n, n_1, n_2)$ is the weight of $(\omega_N, \theta) = (\omega_{mN}^{(i)}, \theta_m(n)^{(i)})$ in Eq. (1) determined from Eqs. (2)–(9), where $k_f$ and $l_d$ are index numbers of wave frequency and direction ($\omega_N = \tilde{\omega}_N(k_f)$ and $\theta = \tilde{\theta}(l_d)$).

The derivative of $D_N$ in Eq. (17) with respect to an ocean wave spectral value at a frequency-direction grid number $(k_p, l_p)$ is

$$\frac{\partial}{\partial G_N(k_p, l_p)} D_N(\omega_{1N}^{(i)}, \omega_{3N}^{(i)}, \omega_{4N}^{(i)}, \theta_1(n)^{(i)}, \theta_3(n)^{(i)}, \theta_4(n)^{(i)})$$

$$= (2\pi)^{-9} C_0(\omega_{1N}^{(i)})^{11} \left( \left\{ 2G_{N1}^{(i)}(n) \left[ \frac{G_{N3}^{(i)}(n)}{(1 + \lambda_{Nl})^4} + \frac{G_{N4}^{(i)}(n)}{(1 - \lambda_{Nl})^4} \right] \right. \right.$$

$$\left. -2\frac{G_{N3}^{(i)}(n)G_{N4}(n)}{(1 - \lambda_{Nl}^2)^4} \right\} \frac{\partial G_{N1}^{(i)}(n)}{\partial G_N(k_p, l_p)}$$

$$+ \left[ \frac{(G_{N1}^{(i)}(n))^2}{(1 + \lambda_{Nl})^4} - 2\frac{G_{N1}^{(i)}(n)G_{N4}^{(i)}(n)}{(1 - \lambda_{Nl}^2)^4} \right] \frac{\partial G_{N3}^{(i)}(n)}{\partial G_N(k_p, l_p)}$$

$$+ \left[ \frac{(G_{N1}^{(i)}(n))^2}{(1 - \lambda_{Nl})^4} - 2\frac{G_{N1}^{(i)}(n)G_{N3}^{(i)}(n)}{(1 - \lambda_{Nl}^2)^4} \right] \frac{\partial G_{N4}^{(i)}(n)}{\partial G_N(k_p, l_p)} \right), \quad (29)$$

$$G_{Nm}^{(i)}(n) = G_N(\omega_{mN}^{(i)}, \theta_m(n)^{(i)}), \quad m = 1, 3, 4 \tag{30}$$

$$\frac{\partial G_{Nm}^{(i)}(n)}{\partial G_N(k_p, l_p)} = \sum_{n_1=1}^{2} \sum_{n_2=1}^{2} w_{Nl} \delta_{(k_\omega + n_1 - 1, l_\theta + n_2 - 1)}^{(k_p, l_p)}, \quad m = 1, 3, 4 \tag{31}$$

where $\delta_{\mathbf{p}}^{\mathbf{q}} = 1$ for $\mathbf{p} = \mathbf{q}$ and $\delta_{\mathbf{p}}^{\mathbf{q}} = 0$ for $\mathbf{p} \neq \mathbf{q}$.

The calculation of the nonlinear source function $S_{NlN}(\omega_N, \theta)$ at $(\omega_N, \theta)$ = $(\tilde{\omega}_N(k_f), \tilde{\theta}(l_d))$ can be summarized as follows. The wave frequencies and directions $(\omega_{mN}^{(i)}, \theta_m(n)^{(i)})$ $(m = 1, \ldots, 4, i = 1, \ldots, 4, n = 1, 2)$ are obtained from Eqs. (18)–(27). The wave spectra $G_{Nm}^{(i)}(n) = G_N(\omega_{mN}^{(i)}, \theta_m(n)^{(i)})$ $(m = 1, \ldots, 4, i = 1, \ldots, 4, n = 1, 2)$ are evaluated from bilinear interpolation using Eqs. (28) and Section 2.2. The nonlinear source function $S_{NlN}(\omega_N, \theta)$ and its derivative with respect to $G_N(k_p, l_p)$ are calculated using Eqs. (17) and (29).

2.4 Wave parameters

The radar-estimated significant wave heights $H_r$, mean periods $T_r$, spectral mean directions $\theta_m$, and frequency spectra $P(f)$ were calculated from radar-estimated wave spectra as

$$H_r = 4E^{1/2} \tag{32}$$

$$E = \int_0^{f_u} \int_{-\pi}^{\pi} F(f, \theta) d\theta df = \int_0^{f_u} P(f) df, \tag{33}$$

$$T_r = E^{-1} \int_0^{f_u} f^{-1} P(f) df, \tag{34}$$

$$\theta_q(f_l) = \mathrm{atan}(Q_s Q_c^{-1}), \tag{35}$$

$$Q_c = Q_c(f_l) = \int_{f_l}^{f_u} \int_{-\pi}^{\pi} \cos\theta F(f, \theta) d\theta df, \tag{36}$$

$$Q_s = Q_s(f_l) = \int_{f_l}^{f_u} \int_{-\pi}^{\pi} \sin\theta F(f,\theta) d\theta df, \qquad (37)$$

where $F(f,\theta) = f_B(2k_0)^2 G_N(\omega_N,\theta)$ is the dimensional wave directional spectrum at the wave frequency $f\ (= f_B\omega_N)$ in Hz and wave direction $\theta$.

The upper limits of integrations $f_u$ in Eqs. (33)–(37) is 0.81 Hz (Hisaki 2014). The spectral mean wave direction is $\theta_m = \theta_q(f_l)$ at $f_l = 0$. The short-wave direction is also evaluated, which is almost determined from the first-order scattering as $\theta_s = \theta_q(f_l)$ at $f_l = 0.47$ Hz, because the frequency $f_l$ is close to the Bragg frequency $f_B = 0.506$ Hz. The radar-estimated wave heights from the dual radar, single radar A, and single radar B are $H_r(\mathrm{D})$, $H_r(\mathrm{A})$, and $H_r(\mathrm{B})$, respectively. Similarly, the radar-estimated wave parameters are written as $T_r(\mathrm{D})$, $T_r(\mathrm{A})$, and $T_r(\mathrm{B})$ (mean wave periods), $\theta_m(\mathrm{D})$, $\theta_m(\mathrm{A})$, and $\theta_m(\mathrm{B})$ (spectral mean wave directions), $\theta_s(\mathrm{D})$, $\theta_s(\mathrm{A})$, and $\theta_s(\mathrm{B})$ (short-wave directions), respectively.

The in-situ observed significant wave heights ($H_s = H_{1/3}$) and periods ($T_s = T_{1/3}$) were observed by the zero-up-crossing method.

## 3 Results

### 3.1 Number of Doppler spectra

The HF radar Doppler spectra data are the same as those of Hisaki (2015). Figure 1 shows the HF radar observation area. Radar A was located at (26.12° N, 127.76° E) and radar B was located at (26.31° N, 127.84° E). The beam directions of radar A and radar B are from 43.5° T to 126° T, and 118.5° T to 201° T, respectively. The beam step is 7.5°, and the number of beam directions for each radar is 12. The radar frequency is 24.5 MHz. The Doppler spectra are sampled on polar regular grids with the origins at the radar position, a range resolution of 1.5 km, and an azimuthal resolution of 7.5°. The radars successively measure in one direction and then change direction for the next measurement. The beam formation is controlled electronically in real time (Hisaki et al., 2001). The Doppler spectra are interpolated with respect to time at two-hour intervals.

The red triangles and blue squares in Figure 1 are the sampling points of the Doppler spectra from radar A and radar B, respectively. However, not all of the Doppler spectra are used for wave estimation. A self-organizing map (SOM) analysis is used to classify the Doppler spectra, and to reject noise-contaminated Doppler spectra. The selection of Doppler spectra is described in Hisaki (2015). The temporal resolution of the observed Doppler spectra was 2 h. The period of analysis was from 0 Local Standard Time (LST) April 17 to 22 LST May 13, 1998. Data were missing for three time series, and 321 time series data were used for the comparison (Hisaki, 2015).

The wave spectra are estimated at $4 \times 4 = 16$ regular grid cells in Figure 1. Cell $(i_x, j_y) = (2, 4)$ is the closest to the in-situ observation point N in Figure 1,

where $i_x$ and $i_y$ $(1 \leq i_x, j_y \leq 4)$ are the cell index numbers for the eastward and northward directions, respectively. The optimization problem with 6080 unknowns (Hisaki 2015) is solved numerically, which requires $1-2$ min per time series data using a personal computer (Intel Core i7-3630QM CPU:2.40GHz, RAM:8GB).

Figure 2a and b show the percentages of the numbers of the Doppler spectra of radar A and radar B that are suitable for wave measurement against the total number of the Doppler spectra that are suitable for the wave measurement. The numbers of the regular cells indicate the time-averaged number of the Doppler spectra for the wave estimation of radar A and radar B, as shown in Figure 6b and c in Hisaki (2015). For example, the mean numbers of the Doppler spectra of radar A and radar B for the wave estimation are $N_{cd}(i_x, j_y)$ =12.8 and $N_{cd}(i_x, j_y) = 7.5$ at $(i_x, j_y) = (2, 3)$, respectively. The percentages of the numbers of the Doppler spectra are $12.8/(12.8+7.5) \simeq 63$ % and $7.5/(12.8+7.5) \simeq 37$ % for radar A (Figure 2a) and radar B (Figure 2b), respectively.

Cells $(i_x, j_y) = (1, 1), (2, 1), (3, 1), (4, 1), (3, 2)$, and $(4, 2)$ are empty-radar Doppler spectrum cells for both radars over the entire period (Figure 2 or Hisaki 2015). An empty-radar Doppler spectrum cell for both radars (or for radar A or radar B) means that the Doppler spectra in the cell for both radars (or for either radar A or radar B) are not used for the wave estimation. Cells $(i_x, j_y) = (2, 1), (4, 3), (1, 4), (2, 4), (3, 4)$, and $(4, 4)$ were the single radar Doppler spectrum cells during the observation period.

The mean numbers of Doppler spectra for the wave estimation from the radar A and radar B per observation are 59.1 and 48.9, respectively. The mean number of the Doppler spectra $N_{cd}(i_x, j_y)$ for the wave estimation from radar A is greatest in cell $(i_x, j_y) = (1, 3)$ and has a value of 17.0 (Figure 2a). The mean number of the Doppler spectra $N_{cd}(i_x, j_y)$ for the wave estimation from radar B has its maximum value in cell $= (2, 4)$ and a value of 11.6 (Figure 2b), which is the closest to the in-situ observation point.

The number of the Doppler spectra of radar A is larger than that of radar B. The number of cells in which the mean $N_{cd}(i_x, j_y)$ is larger than 10 is four cells and one cell for radar A and radar B, respectively. The number of empty-radar Doppler spectrum cells for radar A during the entire observation period is larger than that for radar B. The Doppler spectra of radar A are concentrated in a few regular cells.

## 3.2 Examples of wave spectra comparisons

Figure 3 shows examples of the wave directional spectra estimated from the dual and single radars in the regular cell $(i_x, j_y) = (2, 4)$, which was closest to the in-situ wave observation point. The in-situ observed wave heights $(H_s)$ were 0.63 m and 1.22 m at 14 LST April 26 and 12 LST May 8, respectively. The dual radar-estimated wave heights $(H_r(D))$ were 0.70 m and 1.17 m at those times, respectively. The wave heights estimated from only radar A $(H_r(A))$ were

1.09 m (at 14 LST April 26) and 1.37 m (at 12 LST May 8). The wave heights estimated using only radar A were larger than those dual radar-estimated wave heights for both times (Figure 3a–d).

The spectral peak wave direction is about $\theta = 160°$ in Figure 3a, which means that the dominant wave propagated west-northwestward. The hindcast-dominant wave direction at (26° N, 128° E) from the Japan Meteological Agency (JMA) was from east-southeast at 9 LST (0 UTC) on April 26 (JMA, 1999).

The spectral peak wave direction is about $\theta = -160°$ in Figure 3b, which means that the dominant wave propagated west-northwestward, while JMA hindcast-dominant wave direction was from the east at 9 LST (0 UTC) May 8 (JMA, 1999). Thus, the dominant wave directions of the dual-radar-estimated wave spectra agreed with the directions calculated by JMA.

Figure 4 shows the averaged ocean wave directional spectra during the HF radar observation period. Figure 4a shows the dual-radar-estimated averaged wave spectrum at cell $(i_x, j_y) = (2, 4)$. The wave height $(H_r(\mathrm{D}))$ estimated from the averaged wave spectrum and Eq. (33) was 1.03 m, while the root mean square (rms) value of the in-situ observed significant wave heights was 0.86 m. The dominant wave direction was westward in Figure 4a. The wave period from Eq. (34) and the spectral mean and short-wave direction from Eq. (35) are $T_r(\mathrm{D}) = 6.35$ s, $\theta_m(\mathrm{D}) = 147.2°$, and $\theta_s(\mathrm{D}) = 148.4°$, respectively. Figure 4b shows the dual-radar-estimated averaged wave spectrum of all cells. The 16×321= 5136 wave spectra were averaged, where 321 is the time series number. The wave height estimated from the averaged wave spectrum and Eq. (33) was $H_r(\mathrm{D}) = 1.15$ m, which is higher than that in Figure 4a. The wave period from Eq. (34) and the spectral mean and short-wave direction from Eq. (35) are $T_r(\mathrm{D}) = 6.49$ s, $\theta_m(\mathrm{D}) = 145.9°$, and $\theta_s(\mathrm{D}) = 148.9°$, respectively. The difference between the spectral mean $(\theta_m(\mathrm{D}))$ and the short-wave direction $(\theta_s(\mathrm{D}))$ is small, which shows that the wind wave is dominant in the HF radar observation area and period.

Figure 4c shows the averaged wave spectrum estimated from single radar A at cell $(i_x, j_y) = (2, 4)$. The wave height estimated from the averaged wave spectrum was $H_r(\mathrm{A}) = 1.26$ m, which is higher than that from the dual radar. The spectral peak direction is $\theta = 160°$ in Figure 3c, which is clockwise with respect to that in Figure 3a. The wave period from Eq. (34) and the spectral mean and short-wave direction from Eq. (35) in Figure 4c are $T_r(\mathrm{A}) = 6.80$ s, $\theta_m(\mathrm{A}) = 166.2°$, and $\theta_s(\mathrm{A}) = 168.3°$.

Figure 4d shows the averaged wave spectrum of all cells estimated from single radar A. The wave height, period, spectral mean and short wave directions are $H_r(\mathrm{A}) = 1.22$ m, $T_r(\mathrm{A}) = 6.77$ s, $\theta_m(\mathrm{A}) = 165.6°$, and $\theta_s(\mathrm{A}) = 168.8°$, respectively. The wave height is higher than that in Figure 4c, whereas the wave height in Figure 4b is smaller than that in Figure 4a. The spectral mean and short-wave directions estimated from single radar A are counterclockwise with respect to those from dual radars (Figure 4a and b), i. e., $\theta_m(\mathrm{A}) > \theta_m(\mathrm{D})$ and $\theta_s(\mathrm{A}) > \theta_s(\mathrm{D})$.

Figure 4e and f show averaged wave spectra estimated from single radar B at cell $(i_x, j_y) = (2, 4)$ and at all cells, respectively. The wave heights ($H_r(B)$) from Eq. (33) and wave spectra in Figure 4e and f are 1.04 m and 1.16 m, respectively. The differences in the wave heights from those in the dual-radar case (Figure 4a and b) are small. The wave periods ($T_r(B)$) from Eq. (34) and wave spectra in Figure 4e and f are 6.16 s and 6.21 s, respectively. The spectral mean and short-wave directions from the wave spectrum in Figure 4e are $\theta_m(B)$ = 134.9° and $\theta_s(B)$ = 141.9°, respectively. The spectral mean and short-wave directions from the wave spectrum in Figure 4f are $\theta_m(B)$ = 136.1° and $\theta_s(B)$ = 140.5°, respectively. These values are smaller than those from Figure 4a and b, indicating that the wave directions are clockwise with respect to those estimated from the dual radar. However, the differences between the dual-radar-estimated wave directions and those of single radar B are smaller than the differences between the dual-radar results and those of single radar A: the absolute values of $\theta_m(B) - \theta_m(D)$ and $\theta_s(B) - \theta_s(D)$ are smaller than those of $\theta_m(A) - \theta_m(D)$ and $\theta_s(A) - \theta_s(D)$, respectively.

3.3 Comparisons of wave parameters for the in-situ observation area

Correlation coefficients and rms differences $\langle (X - Y)^2 \rangle^{1/2}$ are used as metrics for comparison, where $X$ and $Y$ are wave parameters, and $\langle \ldots \rangle$ denotes averaging. If $X$ and $Y$ are wave directions, $|X - Y| \leq 180°$. Figure 5 shows the comparisons of the in-situ observed wave parameters and the radar-estimated wave parameters at cell $(i_x, j_y) = (2, 4)$. Figure 5a and b shows a comparison of wave heights. The correlation coefficient between the in-situ observed wave heights and the dual radar-estimated wave heights ($H_r(D)$) was 0.82 with an rms difference of 0.22 m (Hisaki 2015). The correlation of the wave heights estimated from single radar A ($H_r(A)$) is 0.68, with an rms difference of 0.44 m. The wave heights from single radar A are overestimated compared with the dual-radar-estimated wave heights. The correlation of the wave heights estimated from single radar B ($H_r(B)$) with the in-situ observation is 0.76 with an rms difference of 0.25 m. Thus, the wave heights estimated from single radar B are not as overestimated.

Figure 5c and d show comparisons of the wave periods. The correlation coefficient between the in-situ observed significant wave periods and the dual-radar-estimated wave periods from Eq. (34) ($T_r(D)$) was 0.69. The in-situ observed significant wave periods are longer than the energy periods (Eq. (34)), which is consistent with Takahashi et al. (1979).

The correlation coefficients of the radar-estimated wave periods from single radar A ($T_r(A)$) and B ($T_r(B)$) with the in-situ observed significant wave periods were 0.56 and 0.66, respectively. The wave periods estimated from single radar A were longer than those from the dual radar and single radar B.

3.4 Comparison of averaged wave parameters in the entire observation area

Figure 6 shows the mean spatial distributions wave heights, spectral mean wave directions, wave periods, and short-wave directions. These mean wave parameters are estimated from the averaged radar-estimated wave spectra during the observation period. The wave heights are larger and the wave periods are longer in the empty-radar Doppler spectrum cells for both radars. The spectral mean wave directions and short-wave directions are northwestward in all cases: however, these wave directions are directed to the radar in the single radar cases. The spectral mean wave directions and short-wave directions are directed to radar A in Figure 6b and c and to radar B in Figure 6d and e.

Figure 7 shows comparisons of the wave heights and periods estimated from the single and dual radar. The number of samples is 5136. The correlation of the wave heights between the dual radar ($H_r(D)$) and single radar A ($H_r(A)$) is 0.71, and the rms difference between them is 0.22 m. The mean difference in the wave height between single radar A and the dual radar (mean value of $H_r(A)$ $-H_r(D)$) is 0.068 m, demonstrating that the mean wave height estimated from single radar A is higher than that from the dual radar. The correlation of the wave heights between the dual radar ($H_r(D)$) and single radar B ($H_r(B)$) is 0.74, and the rms difference is 0.20 m. The mean difference in the wave heights between the values for single radar B and those for the dual radar (mean value of $H_r(B)$ $-H_r(D)$) is $-0.001$ m. The agreement in the wave heights between single radar B and the dual radar is better than that between single radar A and the dual radar.

The correlation of the wave periods of single radar A is 0.82 and the rms difference is 0.47 s. The mean difference (mean value of $T_r(A)$ $-T_r(D)$) is 0.26 s, and the mean period from single radar A is longer than that from the dual radar. The correlation of the wave periods of single radar B is 0.69 and the rms difference is 0.59 s. The mean difference (mean value of $T_r(B)$ $-T_r(D)$) is $-0.31$ s, and the mean period from single radar B is shorter than that from the dual radar. The differences in the wave heights and periods between the dual radar and the single radar in all cells are smaller than those in cell $(i_x, j_y)$ $= (2, 4)$.

Figure 8 shows comparisons of the spectral mean and short-wave directions estimated from the single and dual radars. The rms difference between $\theta_m(A)$ and $\theta_m(D)$ and the mean difference between them (mean value of $\theta_m(A)$ $-\theta_m(D)$) are 45.9° and 15.1°, respectively (Figure 8a). The positive mean difference is consistent with Figure 4b and c, which means that the spectral mean wave directions estimated from single radar A are directed to that radar A in comparison with the dual radar-estimated wave directions. The rms and mean difference (mean value of $\theta_m(B)$ $-\theta_m(D)$) between the dual radar and single radar B are 38.8° and $-2.2$°, respectively (Figure 8b). The negative mean difference is also consistent with Figure 4b and f.

Figure 8c shows comparisons of the short-wave directions estimated from single A and the dual radar. The rms and mean difference (mean value of $\theta_s(A)$ $-\theta_s(D)$) between the dual radar and single radar A are 51.0° and 16.6°,

respectively. Figure 8d shows comparisons of the short-wave directions for single radar B and the dual radar. The rms and mean difference $(\theta_s(\mathrm{B}) - \theta_s(\mathrm{D}))$ of the dual radar and single radar B are $38.0°$ and $1.2°$, respectively. The differences in the spectral mean and short-wave directions between single radar A and the dual radar are larger than those between single radar B and the dual radar. In particular, the plots around the line $\theta_m(\mathrm{A}) + \theta_m(\mathrm{D}) = \pm 180°$ $(\theta_s(\mathrm{A}) + \theta_s(\mathrm{D}) = \pm 180°)$ can be seen in the case of single radar A (Figure 8a and c). As a result, the differences between the single radar-A-estimated wave directions and the dual-radar-estimated wave directions are larger than those between the single-radar-B-estimated wave directions and those estimated from dual radar.

3.5 Comparisons of wave heights and periods in each cell

Figure 9 shows time series of radar-estimated wave heights ($H_r(\mathrm{D})$, $H_r(\mathrm{A})$, and $H_r(\mathrm{B})$) and periods ($T_r(\mathrm{D})$, $T_r(\mathrm{A})$ and $T_r(\mathrm{B})$) at cell $(i_x, j_y) = (1,3)$, $(2,3)$, and $(3,3)$. The Doppler spectra are present for both radar A and radar B, but there are many more Doppler spectra for radar A than for radar B at $(i_x, j_y) = (1,3)$. There are a good number of the Doppler spectra from both radar A and radar B at cell $(i_x, j_y) = (2,3)$, but there is a larger number of the Doppler spectra for radar A than for radar B. There are few Doppler spectra for both radar A and radar B at cell $(i_x, j_y) = (3,3)$, but the number of the Doppler spectra is larger for radar B than for radar A (Figure 2).

There are several cases in which the wave data are not estimated adequately. For example, the dual-radar-estimated wave heights in the cell at $(1,3)$ on 8 LST 23 April are too high (Figure 9a): this result is due to the inadequate convergence of the iteration.

The agreement between $H_r(\mathrm{A})$ (green) and $H_r(\mathrm{D})$ (red) in Figure 9a and b appears to be better than that between $H_r(\mathrm{B})$ (blue) and $H_r(\mathrm{D})$, whereas the agreement of $H_r(\mathrm{B})$ with $H_r(\mathrm{D})$ seems to be better than that of $H_r(\mathrm{A})$ with $H_r(\mathrm{D})$ in Figure 9c. The agreement between $T_r(\mathrm{A})$ (green) and $T_r(\mathrm{D})$ (red) seems to be better than that between $T_r(\mathrm{B})$ (blue) and $T_r(\mathrm{D})$, in Figure 9d–f. In addition, the plots of the radar-estimated wave periods from single radar A ($T_r(\mathrm{A})$) in Figure 9d–f seem to agree with each other. The plots of $T_r(\mathrm{D})$ also appear to be consistent.

Figure 10 shows the comparison of the wave heights in each regular cell. The spatial pattern of the rms differences of the wave heights is opposite to that of the correlations. If the correlation of wave heights is high for a cell, the rms difference of the wave heights is low for that cell. The higher correlation is related to the lower rms difference. The correlation of the wave heights between single radar A ($H_r(\mathrm{A})$) and the dual radar ($H_r(\mathrm{D})$) is 0.86, with the highest value at $(i_x, j_y) = (2,2)$. The correlation at $(i_x, j_y) = (2,4)$, which is the closest to the in-situ observation point, is 0.68, which is a low value. The correlations range from 0.64 to 0.86 (Figure 10a).

The mean values of $H_r(A) - H_r(D)$ are positive in all of the regular cells, demonstrating that the mean single-radar A-estimated wave heights are higher than the mean dual-radar-estimated wave heights. The difference is 0.23 m at $(i_x, j_y) = (2, 4)$, which is the largest value. The mean differences range from 0.018 m to 0.23 m: most of the differences are less than 0.1 m (Figure 10b).

The correlation of the wave heights between single radar B ($H_r(B)$) and the dual radar ($H_r(D)$) is 0.88 at $(i_x, j_y) = (2, 4)$, which is the highest value. The correlation at $(i_x, j_y) = (2, 2)$, where the dual radar to single radar A correlation is the highest, is 0.60, which is the lowest correlation for single radar B (Figure 10c).

The mean differences in the wave heights in Figure 10d are smaller than those in Figure 10b. All of the absolute values of mean differences are less than 0.1 m, and half are less than 0.01 m. The mean difference at $(i_x, j_y) = (2, 3)$ is $-0.062$ m, which is the maximum absolute value of the difference (Figure 10d).

Figure 11 shows the comparison of the wave periods in each regular cell. The correlation of the wave periods between single radar A ($T_r(A)$) and the dual radar ($T_r(D)$) has a maximum value of 0.87 and at $(i_x, j_y) = (2, 2)$, and a minimum value of 0.78 at $(i_x, j_y) = (1, 3)$ (Figure 11a).

The mean differences in the wave periods (mean values of $T_r(A) - T_r(D)$) are positive in all of the cells, which means that the wave periods from single radar A are longer than those from the dual radars. The largest difference is 0.45 s at $(i_x, j_y) = (2, 4)$ (Figure 11b), where the correlation is low (Figure 11a): the lowest difference is 0.18 s at $(i_x, j_y) = (3, 2)$.

The maximum correlation between $T_r(B)$ and $T_r(D)$ is 0.81 at $(i_x, j_y) = (3, 4)$. The minimum correlation of the wave periods is 0.59 at $(i_x, j_y) = (2, 2)$ (Figure 11c), where the correlation between $T_r(A)$ and $T_r(D)$ is the highest.

The mean differences of the periods are negative in all cells, which means that the wave periods obtained from single radar B are shorter than those from the dual radar. The maximum difference is $-0.535$ s at $(i_x, j_y) = (1, 3)$, and the minimum difference is $-0.181$ s at $(i_x, j_y) = (2, 4)$ (Figure 11d). The cells with the maximum and minimum difference are different from those with cells of the minimum and maximum correlation. However, the correlation is 0.66 and low at $(i_x, j_y) = (1, 3)$, and 0.80 and high at $(i_x, j_y) = (2, 4)$ (Figure 11c). The wave directions are also compared for each cell (Figure 12): this is discussed in Section 4.4.

## 4 Discussion

### 4.1 Wave height and period

Wave data from the single and dual HF radar arrays are compared with each other. The iteration of the final step (Section 2.1) for solving the nonlinear optimization problem in the single radar case is less stable than that of the dual radar case.

Changes in the seed used to gerenate random numbers in the first step and reiterations due to the inadequate convergence of the iteration (Section 2.1) were performed several times for the single radar cases. The iteration of the final step seeks the local minimum of the objective function instead of the global minimum. Therefore, the solution may be inadequate if the initial guess is inadequate. In some cases, the dual-radar estimated wave heights or periods are inadequate (Figure 9); thus, the criterion for recomputation to solve the nonlinear optimization problem must be improved.

Radar A can be characterized as having larger number of the Doppler spectra for the wave estimation but a smaller coverage of the Doppler spectrum area . The number of regular cells in which $N_{cd}(i_x, j_y)$ is 0 for the radar A is larger than the equivalent number for radar B.

The number of the Doppler spectra for the wave estimation from radar A is $N_{cd}(i_x, j_y) = 0$ for $(i_x, j_y) = (2, 4)$, the closest cell to the in-situ observation point. The number of the Doppler spectra for wave estimation from radar B is not 0 at the regular cell.

In a previous study, the correlation of 25-MHz radar-estimated wave heights with in-situ observed wave heights was 0.97, and the rms differerence is 0.45 m (Wyatt et al., 2011). Both the correlation and the rms difference are smaller for the present method, but the range of the wave heights in the present study is smaller than that in Wyatt et al. (2011). The radar-estimated periods, which are the energy period (Eq. (34)), are shorter than the significant wave periods $T_{1/3}$ (Takahashi et al., 1979), and the radar-estimated periods $T_r$ are shorter than the in-situ observed periods (Figure 5c).

The ranking of the accuracy of radar-estimated wave parameters at cell $(i_x, j_y) = (2, 4)$ is in the order of dual-radar-estimated wave parameters, single-radar B-estimated wave parameters, and single-radar A-estimated wave parameters from greatest to least accuracy. The wave heights and periods from single radar A at that cell, which is an empty-radar Doppler spectrum cell for that radar, are significantly overestimated.

The differences in the dual- and single-radar-estimated wave heights and periods in all cells are smaller than those for cell $(i_x, j_y) = (2, 4)$. However, there are differences in the details. The difference from the dual-radar-estimated wave heights is smaller for single radar B than for single radar A for all cells. The correlation of the dual-radar-estimated wave heights with the single-radar-B-estimated wave heights is higher than that with the single-radar-A-estimated wave heights. In contrast, the correlation of the wave periods estimated from the dual radar with those from single radar B is lower than the correlation of the dual radar with single radar A.

A possible explanation follows for the result that the correlation of $H_r(\text{D})$ with $H_r(\text{B})$ is higher than that of $H_r(\text{D})$ with $H_r(\text{A})$, whereas the correlation of $T_r(\text{D})$ with $T_r(\text{A})$ is higher than that of $T_r(\text{D})$ with $T_r(\text{B})$. The contributions of the spatial and temporal variability of the wave heights to the total variability of the wave heights are different from those of the wave periods. The time-mean value of the standard deviations of the spatial variability of the dual-radar-estimated wave heights is 0.116 m, which means that the averaged spatial

variability of the wave heights in the radar observation area is approximately 0.12 m. The spatial mean value of the standard deviations of the temporal variability is 0.256 m, which means that the averaged temporal variability of the wave heights in the radar observation period is about 0.26 m. The ratio of these values is $0.256/0.116 \simeq 2.2$.

The time-mean value of the standard deviations of the spatial variability of the dual-radar-estimated wave periods is 0.205 s, and the spatial-mean value of standard deviations of the temporal variability is 0.652 s. The ratio of these two values is $0.652/0.205 \simeq 3.18$. The contribution of the spatial variability to the spatio-temporal variability of the wave heights is larger than that of the wave periods. Therefore, the difference in the wave heights between single radar B, which covers a wider area of the Doppler spectra (Figure 2), from the dual-radar-estimated wave heights is smaller the difference between single radar A and the dual radar. On the other hand, the difference in the wave periods between single radar A, which uses a larger number of the Doppler spectra, and the dual radar is smaller than that between single radar B and the dual radar.

## 4.2 Wave direction

The short-wave directions estimated from the first-order scattering in 1.5-km grids are also almost unidirectional (Hisaki 2002). The wave directions in Figure 6 are more uniform because of averaging of the Doppler spectra in space and because of the regularization constraint ((c6) in Section 2.1).

There is a tendency for both the spectral mean and the short-wave directions estimated from a single radar to be directed to the radar direction. We explain this tendency in the case of the short-wave direction, which is almost determined from the first-order scattering and which is simple, as follows.

The first-order scattering has two peaks, at the positive and negative Bragg frequencies. The normalized first-order scattering ((c1) in Section 2.1) is the ratio of the larger first-order scattering to the sum of the two first-order scatterings

$$r_f(\theta_b) = \frac{\text{Larger first}-\text{order scattering}}{\text{Sum of the first}-\text{order scattering}} \tag{38}$$

or equation (2) in Hisaki (2006), where $\theta_b$ is the wave direction with respect to the beam direction.

The value of $r_f(\theta_b)$ (Eq. (38)) is 1/2 and minimum at $\theta_b = \pi/2$ theoretically because both first-order peaks are the same level as each other. The value of $r_f(\theta_b)$ is 1 and maximum at $\theta_b = \pi$ theoretically. The derivative of $r_f(\theta_b)$ with respect to $\theta_b$ is 0 at $\theta_b = \pi$. The second-order derivative $d^2 r_f(\theta_b)/d\theta_b^2$ is negative around $\theta_b = \pi$, and the curve of $r_f$ with respect to $\theta_b$ is convex upward in the $\theta_b - r_f$ plane around $(\theta_b, r_f) = (\pi, 1)$. The inverse function of $r_f = r_f(\theta_b)$ is $\theta_b = \theta_b(r_f)$, which is convex downward in the $r_f - \theta_b$ plane around $(r_f, \theta_b) = (1, \pi)$. The mean position of the plots on the $\theta_b = \theta_b(r_f)$ curve is

above the curve in the $r_f - \theta_b$ plane because the curve is convex downward. Therefore, the value of $\theta_b$ estimated from the single radar is closer to $\pi$.

There is an exception to this tendency in Figure 8d, which shows that the mean difference $(\theta_s(B) - \theta_s(D))$ between the dual radar and single radar B is positive, while the short-wave directions from the averaged wave spectrum in Figure 4b and f are $\theta_s(D) = 148.9°$ and $\theta_s(B) = 140.5°$, respectively. This inconsistency between the difference in the short-wave directions from the averaged wave spectra and that from the scatter plot (Figure 8d) shows that the bias of the single radar-estimated wave direction to the radar is insignificant at lower wave height conditions. Wind speeds are not high and wind directions are fluctuating at lower wave height conditions. The Doppler spectra are sampled at different times and are interpolated with respect to time; thus, fluctuations in the short-wave directions cannot be retrieved.

The great difference in the wave direction between the dual radar and the single radar is mainly due to the left-right directional ambiguity. The left-right ambiguity of the single-radar-A-estimated wave direction with respect to the beam direction is more prominent than that for single radar B. The radar beam coverage area of radar B is wider than that of radar A (Figures 1 and 2). Therefore, the possibility that the left-right ambiguity is unresolved is higher for single radar A than for single radar B.

4.3 Comparisons of wave height and period for each cell

If the correlation between $H_r(A)$ and $H_r(D)$ is high in a cell, the absolute value of the difference between $H_r(A)$ and $H_r(D)$ is low at that cell, and the correlation between $H_r(B)$ and $H_r(D)$ is low at that cell. This tendency is also true for the wave period.

A Doppler spectrum averaged from many Doppler spectra contributes to the solution of the nonlinear optimization problem more significantly than one averaged from a few Doppler spectra because the weights of constraints (c1) and (c2) in the objective function are dependent on the number of the Doppler spectra available for averaging (Section 2.1). The differences in the wave heights (Figure 10) and periods (Figure 11) between the dual radar and the single radar are dependent on the number of ratios of the Doppler spectra for the wave estimation (Figure 2). For example, the correlation of the dual-radar-estimated wave heights with those from single radar A is highest at $(i_x, j_y) = (2, 2)$ (Figure 10a); the ratio of the number of the Doppler spectra from radar A is also highest for that cell (Figure 2a).

The correlation between the correlations in Figure 10a and the percentages of the Doppler spectra of radar A that are suitable for the wave measurement (Figure 2a) from 12 cells, which are not empty-radar Doppler spectrum cells for at least one radar, is 0.91. The correlation between the correlations in Figure 10c and the percentages of the Doppler spectra for radar B (Figure 2b) is 0.78. The correlations of the absolute values of the mean differences (Fig-

ure 10b and c) with percentages for radar A and radar B (Figure 2) are $-0.72$ and $-0.91$, respectively.

The correlations for the numbers of the Doppler spectra are lower than those for percentages. For example, the correlation between correlations in Figure 10a and the number of the Doppler spectra for radar A (numbers in Figure 2a) for 12 cells is 0.62. The correlation between Figure 10d and the number of the Doppler spectra for radar B (numbers Figure 2b) is 0.056, which is low. The differences in the wave heights between the dual radar and the single radar are related to the percentages of the number of the Doppler spectra for the wave estimation rather than the numbers of the Doppler spectra.

The differences in the wave periods between from the single radar and from the dual radar are also related to the percentages of the number of the Doppler spectra for the wave estimation. The correlations of percentages in Figure 2a with the correlations in Figure 11a, and with absolute values of the mean differences in in Figure 11b, are 0.66 and $-0.79$, respectively, which are estimated from 12 cells. The correlations for radar B are 0.77 and 0.42, respectively. Only the correlation between the mean differences of the wave periods and percentages of the Doppler spectra of single radar B is not so high. The wave periods are more homogeneous than the wave heights, as discussed in Section 4.1. The wave period in a cell is more affected by the wave spectra of the surrounding cells than is the wave height.

4.4 Comparisons of wave direction for each cell

The differences between the wave directions estimated from the dual radar and the single radar are mainly due to the failure to resolve the left-right ambiguity with respect to the beam direction. The radar-estimated spectral mean wave directions are almost unidirectional spatially. There are no cases in which the left-right ambiguity is resolved for one cell while the left-right ambiguity is simultaneously unresolved for another cell.

The relationship between the differences of the single-radar-estimated wave directions from the dual-radar-estimated wave directions (Figure 12) and the numbers or ratios of the Doppler spectra in the cell (Figure 2) is also investigated.

The relationships are unclear, although some pairs of parameters show relationships. For example, the correlation between the rms differences of $\theta_m(D)$ from $\theta_m(A)$ (Figure 12a) and the numbers of the Doppler spectra (Figure 2a) is 0.64 for 16 cells. The correlation between rms differences of $\theta_m(D)$ from $\theta_m(B)$ (Figure 12d) and numbers of Doppler spectra of 16 cells (Figure 2b) is 0.79. The spatial variability of the difference of $\theta_m(D)$ with $\theta_m(A)$ or with $\theta_m(B)$ is mainly due to the sampling variability of Doppler spectra, and the difference is related with the number of Doppler spectra.

The relationships between the differences between $\theta_s(D)$ and $\theta_s(A)$ or $\theta_s(D)$ and $\theta_s(B)$ and the numbers of the Doppler spectra of the cells are more unclear than those of $\theta_m$. For example, the correlation between the rms differences of

$\theta_s(D)$ and $\theta_s(A)$ and the numbers of the Doppler spectra for the wave estimation is 0.61. The correlation of those parameters for $\theta_s(B)$ is 0.31. The difference between the dual- and single-radar-estimated short-wave direction is not only due to the failure to resolve the left-right ambiguity but also fluctuations in the wind directions. The spatial variability of the short-wave differences is affected by the spatial variability of the wind direction. The beam formation is controlled in real time, and the Doppler spectra are interpolated with respect to time. The radar-estimated short-wave directions do not capture the spatial variability of the short-wave directions when the wind directions are fluctuating.

## 5 Conclusion and Future Research

The conclusions of this study can be summarized as follows. It is demonstrated that HIAS can be applied to both dual and single radar systems. The agreement of the dual-radar-estimated wave heights with those estimated from the single radar is better for radar B than for radar A, demonstrating that the agreement is better for the case wherein the area of the Doppler spectra of the single radar is wider than in the case wherein the number of Doppler spectra of the single radar is larger. The dual-radar-estimated-wave periods show better agreement with the single-radar-A-estimated wave periods than those estimated from single radar B, demonstrating that the number of Doppler spectra of the single radar is more critical for agreement than the area of the Doppler spectra. The left-right ambiguity in the single-radar-estimated wave direction can be resolved if the Doppler spectra are obtained from a wider area. Differences in the wave heights and periods obtained from the single and dual radars are related to the percentages of the numbers of Doppler spectra suitable for the wave estimation.

We demonstrate that HIAS can be applied to the single radar case if the area of the Doppler spectra is sufficiently wide. However, there is room for improvement in the method. We address one of the subjects related to the number of Doppler spectra and expansion of the area of the Doppler spectra for the wave estimation. Herein, we used only the Doppler spectra for which both the first- ((c1) in Section 2.1) and second-order scattering ((c2) in Section 2.1) could be used. However, although the second-order scattering is contaminated by noise, it is possible to use only the first-order scattering. This improvement will be explored in future work.

# References

1. Barrick, D. E., (1971), Dependence of second-order sidebands in HF sea echo upon sea state. Proc. Antennas and Propagation Society Int. Symp., Los Angeles, CA, IEEE, 194–197. doi:10.1109/APS.1971.1150934.
2. Barrick, D. E., and B. L. Weber, (1977), On the nonlinear theory for gravity waves on the ocean's surface. Part II: Interpretation and applications. J. Phys. Oceanogr., 7, 11–21. doi: 10.1175/1520-0485(1977)007<0011:OTNTFG>2.0.CO;2.
3. de Valk C, A. Reniers, J. Atanga. A. Vizinho, and J. Vogelzang (1999). Monitoring surface waves in coastal waters by integrating HF radar measurement and modelling. Coastal Eng., 37, 431–453, doi:10.1016/S0378-3839(99)00037-X.
4. Gill E. W., and J. Walsh, (2001), High-frequency bistatic cross sections of the ocean surface. Radio Sci., 36, 1459–1475, doi: 10.1029/2000RS002525.
5. Gill E. W., W. Huang, J. Walsh, (2006), On the development of a second-order bistatic radar cross section of the ocean surface: A high-frequency result for a finite scattering patch, IEEE J. Oceanic Eng., 31, 740–750. doi: 10.1109/JOE.2006.886228.
6. Gurgel K.-W., H.-H. Essen, T. Schlick (2006), An empirical method to derive ocean waves from second-order Bragg scattering: prospects and limitations. IEEE J. Ocean. Eng., 31(4), 804–811. doi: 10.1109/JOE.2006.886225.
7. Hashimoto N. and M. Tokuda (1999). A Bayesian approach for estimation of directional wave spectra with HF radar. Coast. Eng. J., 41(2), 137-149, doi: 10.1142/S0578563499000097.
8. Hasselmann, S., K. Hasselmann, J. A. Allender, and T. P. Barnet (1985), Computations and parameterizations of the nonlinear energy transfer in a gravity wave spectrum. Part II: parameterization of the nonlinear transfer for application in wave models. J. Phys. Oceanogr.,15, 1378–1391. doi: 10.1175/1520-0485(1985)015<1378:CAPOTN>2.0.CO;2.
9. Hisaki, Y. (1999) Correction of amplitudes of Bragg lines in the sea echo Doppler spectrum of an ocean radar. J. Atmos. Oceanic Technol, 16, 1416–1433. doi: 10.1175/1520-0426(1999)016<1416:COAOBL>2.0.CO;2.
10. Hisaki, Y. (2002) Short-wave directional properties in the vicinity of atmospheric and oceanic fronts. J. Geophys. Res., 107, 11, doi:10.1029/2001JC000912.
11. Hisaki, Y. (2005) Ocean wave directional spectra estimation from an HF ocean radar with a single antenna array: Observation. J. Geophys. Res. 10, doi: 10.1029/2005JC002881.
12. Hisaki, Y. (2006) Ocean wave directional spectra estimation from an HF ocean radar with a single antenna array: Methodology. J. Atmos. Oceanic Technol., 23, 268–286, doi: 10.1175/JTECH1836.1.
13. Hisaki Y. (2009) Quality control of surface wave data estimated from low signal-to-noise ratio HF radar Doppler spectra. J. Atmos. Oceanic Technol., 26,. 2444-2461. doi:10.1175/2009JTECHO653.1.
14. Hisaki Y. (2013) Classification of surface current maps. Deep-Sea Res., Part I, 73, 117-126. doi: 10.1016/j.dsr.2012.12.001.
15. Hisaki Y., (2014) Intercomparison of wave data obtained from single high-frequency radar, in-situ observation and model prediction. Int. J. Remote Sensing., 35, 3459-3481, doi:10.1080/01431161.2014.904971.
16. Hisaki Y. (2015) Development of HF radar inversion algorithm for spectrum estimation (HIAS). J. Geophys. Res. 120. doi: 10.1002/2014JC010548.
17. Hisaki, Y., and C. Imadu. (2009) The southward recirculation of the East China Sea Kuroshio west of the Okinawa Island, J. Geophys. Res. doi:10.1029/2008JC004943.
18. Hisaki. Y., and M. Tokuda (2001) VHF and HF sea echo Doppler spectrum for a finite illuminated area. Radio Sci., 36, 425–440, doi: 10.1029/2000RS002343.
19. Hisaki, Y., W. Fujiie, T. Tokeshi, K. Sato, S. Fujii (2001) Surface current variability east of Okinawa Island obtained from remotely sensed and in-situ observational data. J. Geophys. Res. 106, 31057–31073. doi: 10.1029/2000JC000784.
20. Hisaki Y., M. Kashima, S. Kojima (2016). Surface current patterns observed by HF radar: Methodology and analysis of currents to the north of the Yaeyama Islands, East China Sea. Ocean Dynamics, 66, 329–352. doi: 10.1007/s10236-016-0924-4.
21. Howell, R., and J. Walsh (1993), Measurement of ocean wave spectra using narrow-beam HF radar. IEEE. J. Ocean. Eng., OE-18, 296–305. doi: 10.1109/JOE.1993.236368.

22. Japan Meteological Agency (1999), Annual report on ocean waves 1998. *3*, Japan Meteological Agency, Tokyo.
23. Takahashi T., M. Hirose, T. Sasaki (1979), Relationship between spectral width parameters and wave statics. Technical Note of the Port and Harbour Research Institute Ministry of Transportation, No. 315, 65 pp (in Japanese). Available on line at: http://www.pari.go.jp/search-pdf/no0315.pdf.
24. Wyatt, L. R. (1990), A relaxation method for integral inversion applied to HF radar measurement of the ocean wave directional spectra. Int. J. Remote Sensing, 11, 1481–1494. doi: 10.1080/01431169008955106.
25. Wyatt L. R., J. J. Green, A. Middleditch, 2011. HF radar data quality requirements for wave measurement. Coastal Eng.,58, 327–336. doi:10.1016/j.coastaleng.2010.11.005.
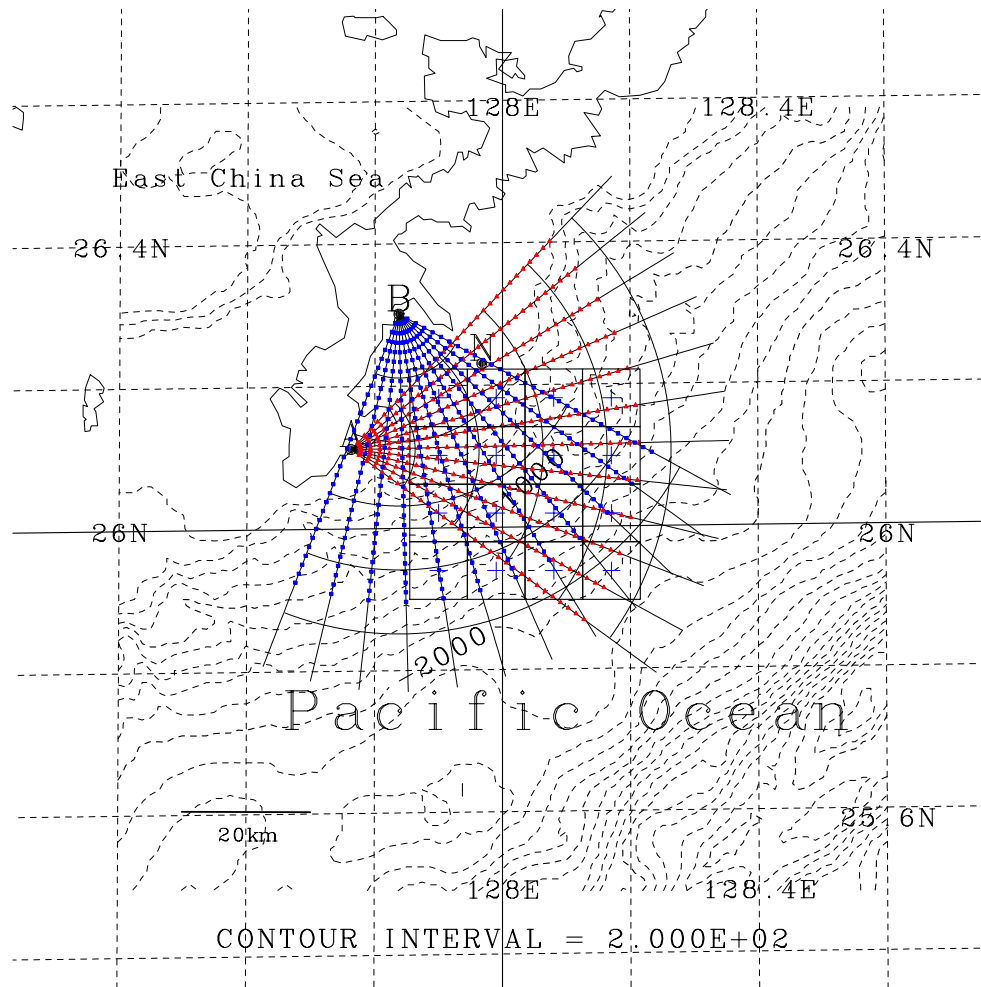
**Fig. 1** Map of the HF radar observation area. The island of the radar location is the Okinawa Island.
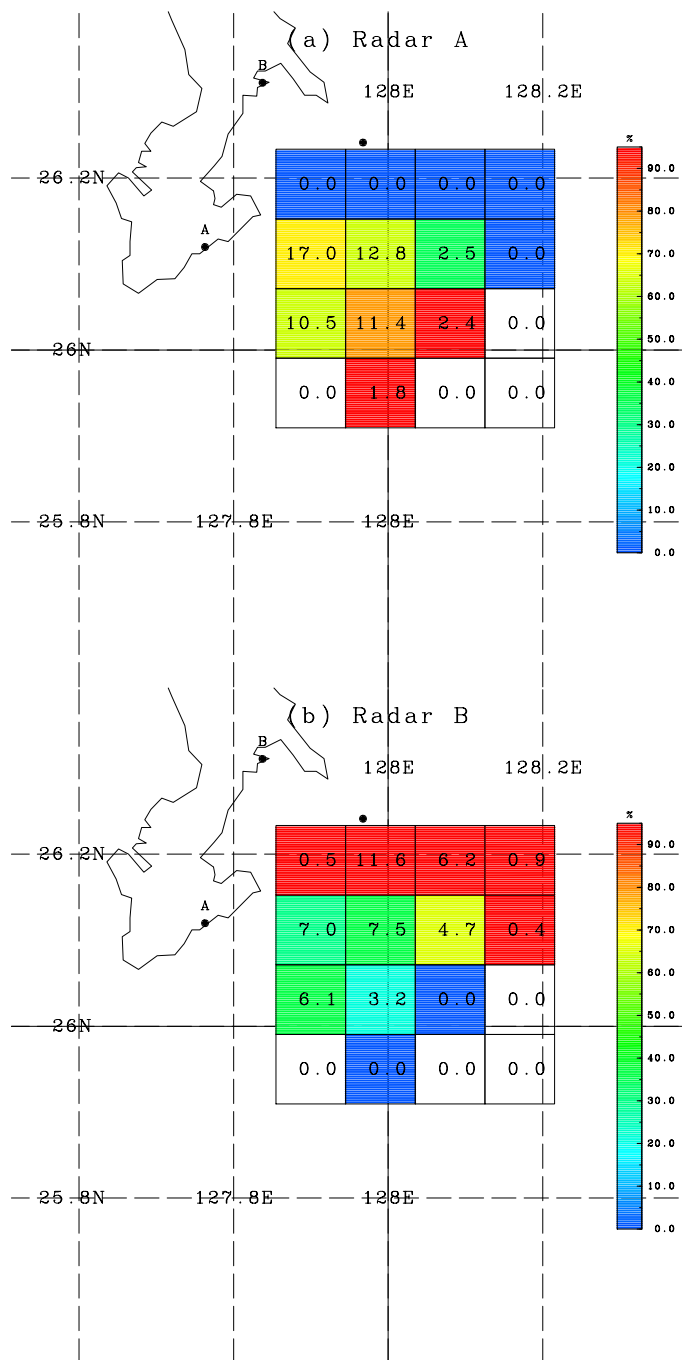
**Fig. 2** Percentages of the numbers of the Doppler spectra of (a) radar A and (b) radar B that are suitable for wave measurement against the total number of the Doppler spectra that are suitable for the wave measurement. The numbers in the cells are the average numbers of Doppler spectra for wave estimation per observation.
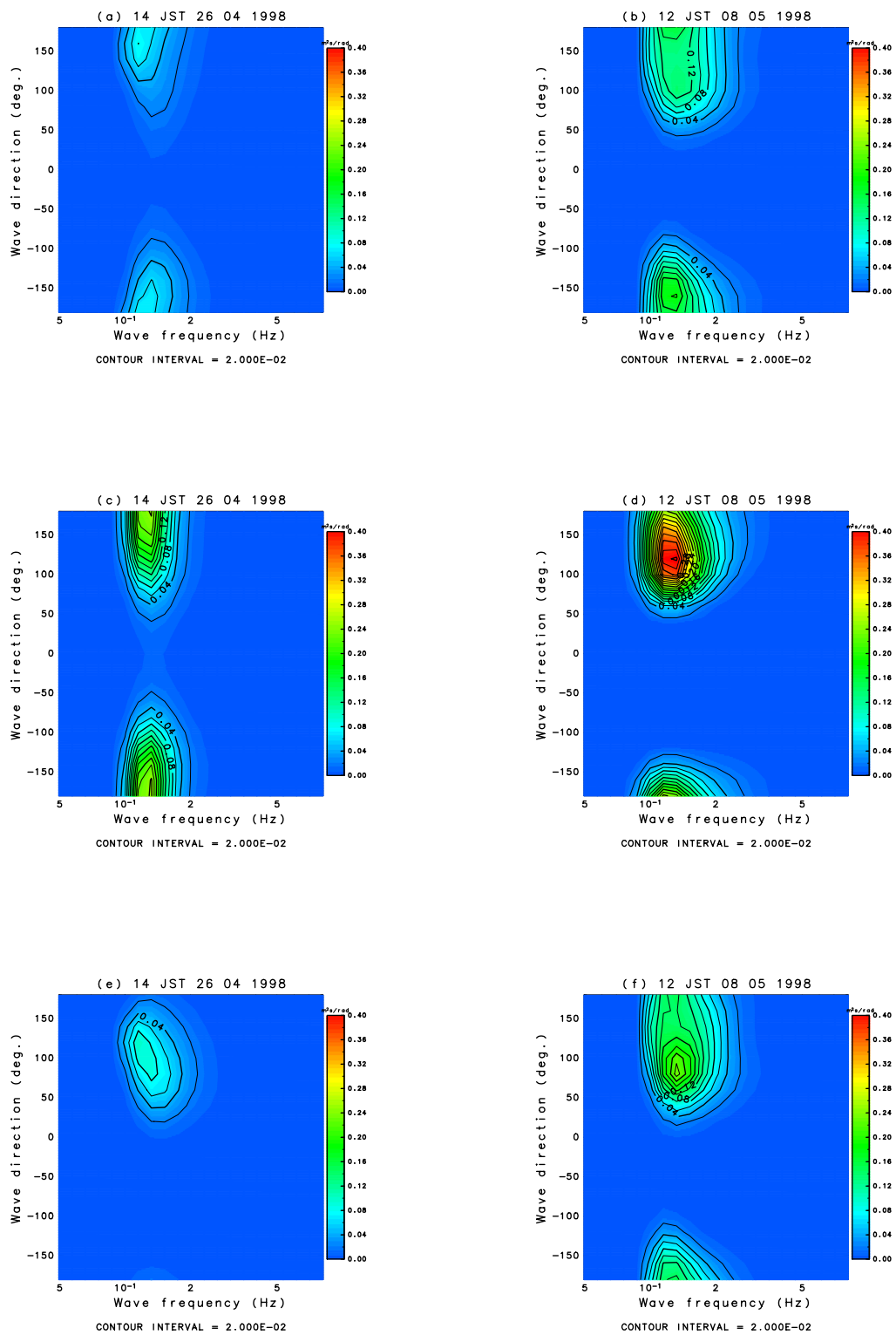
**Fig. 3** Examples of dual-radar-estimated ocean wave spectra $F(f, \theta)$ ($f = \omega/(2\pi)$) in cell $(i_x, j_y) = (2, 4)$ at (a) 14 LST April 26 and (b) 12 LST May 8, 1998. (c) As (a) but for single radar A. (d) As (b) but for single radar A. (e) As (a) but for single radar B. (f) As (b) but for single radar B.
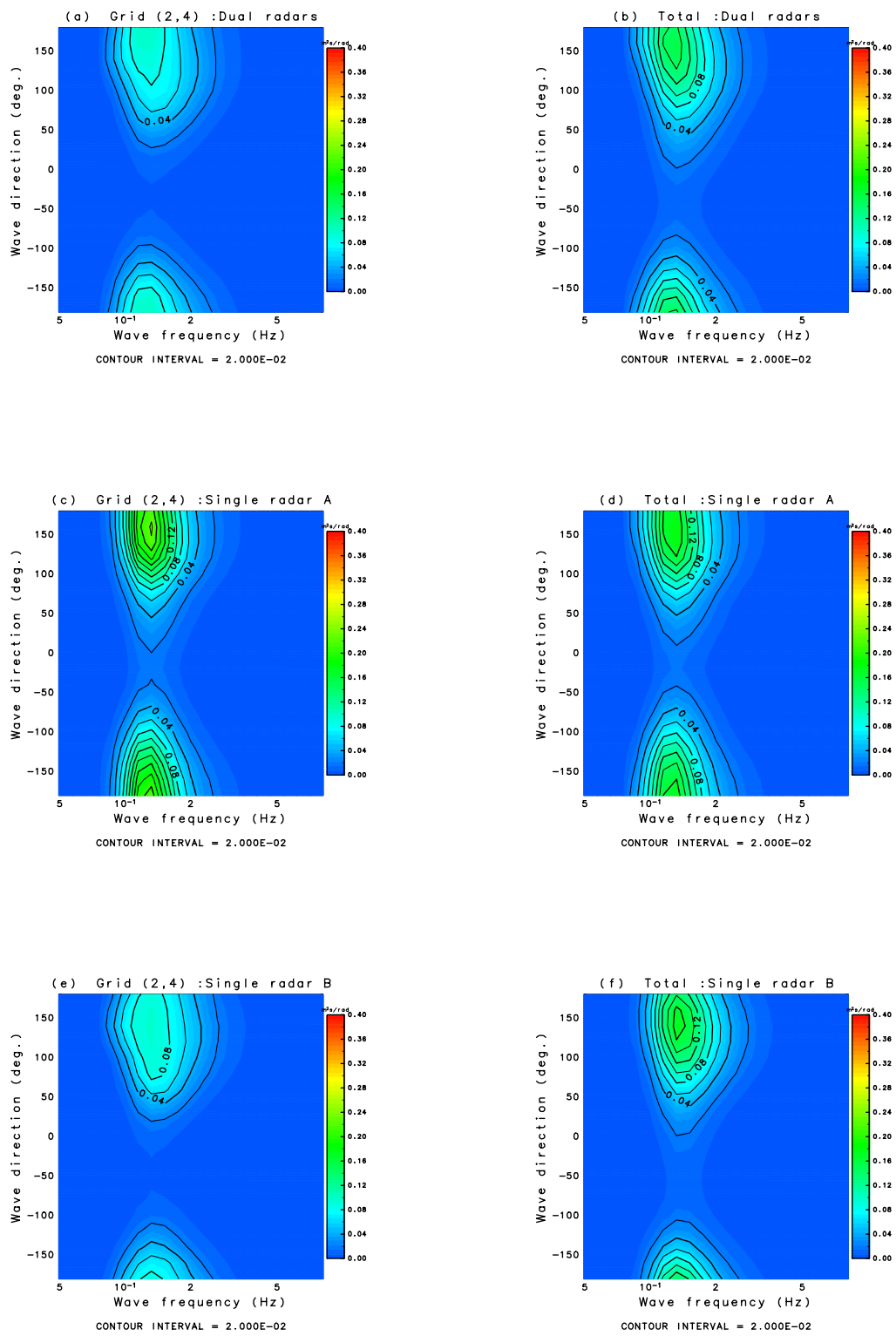
**Fig. 4** Averaged wave spectrum during the observation period (a) in cell $(i_x, j_y) = (2, 4)$ estimated from the dual radar. (b) Same as (a) but averaged over all radar cells. (c) As (a) but estimated from single radar A. (d) As (b) but estimated from single radar A. (e) As (a) but estimated from single radar B. (f) As (b) but estimated from single radar B.
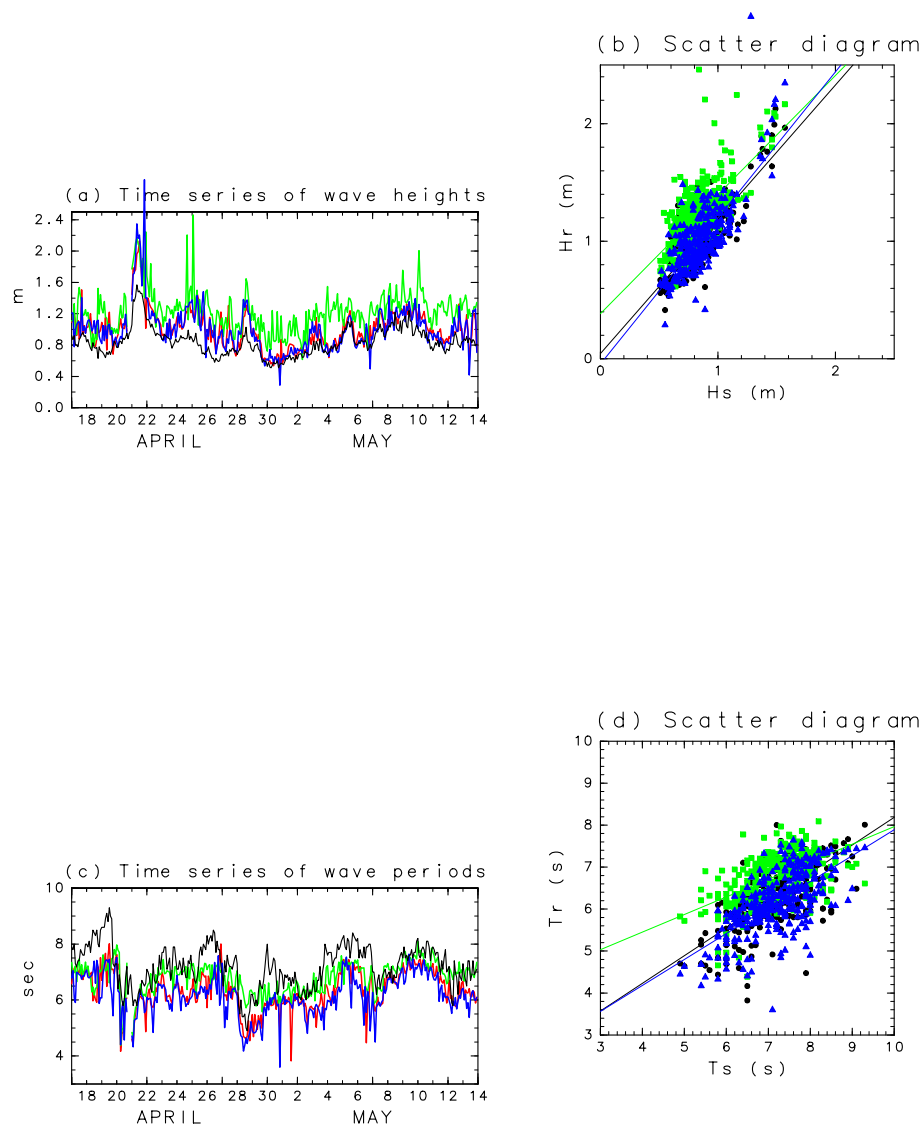
**Fig. 5** (a) Time series of wave heights from in-situ observation (black), dual radar (red), single radar A (green), and single radar B (blue). (b) Scatter plots of in-situ observed wave heights ($H_s = H_{1/3}$) and dual-radar-estimated wave heights (black), of in-situ observed wave heights and wave heights estimated from single radar A (green), and of in-situ observed wave heights and wave heights estimated from single radar B (blue). (c) As (a) but for in-situ observed significant wave periods ($T_s = T_{1/3}$) and radar-estimated spectrum mean periods. (d) As (b) but for the in-situ observed significant wave periods and radar-estimated spectrum mean periods.
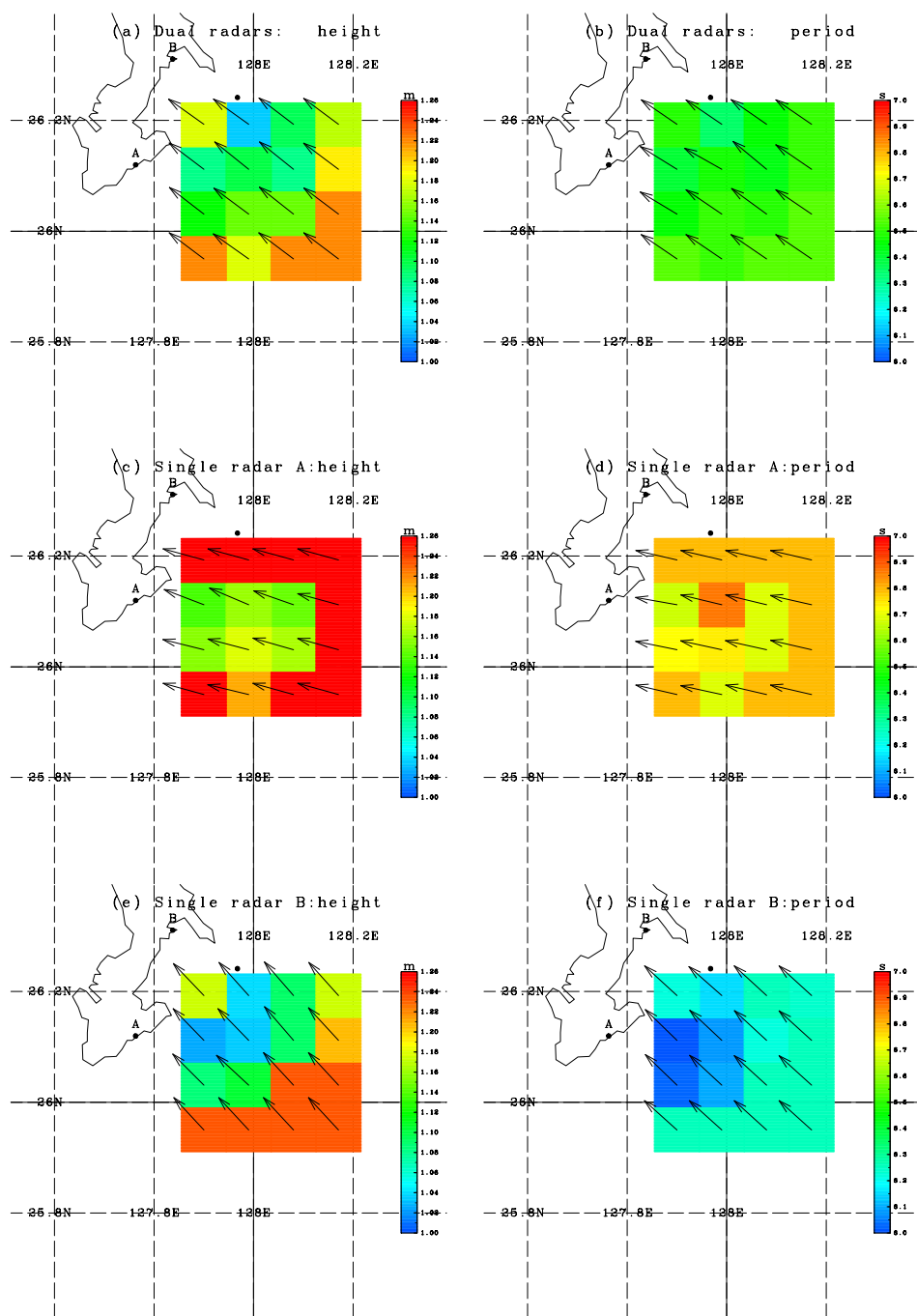
**Fig. 6** (a) Wave heights ($H_r(\mathrm{D})$) and spectral mean directions ($\theta_m(\mathrm{D})$) from averaged dual-radar estimated spectra. (b) Wave periods ($T_r(\mathrm{D})$) and short-wave directions ($\theta_s(\mathrm{D})$) from averaged dual-radar-estimated spectra. (c) As (a) but from single radar A ($H_r(\mathrm{A})$ and $\theta_m(\mathrm{A})$). (d) As (b) but from single radar A ($T_r(\mathrm{A})$ and $\theta_s(\mathrm{A})$). (e) As (a) but from single radar B ($H_r(\mathrm{B})$ and $\theta_m(\mathrm{B})$), and (f) same as (b) but from single radar B ($T_r(\mathrm{B})$) and $\theta_s(\mathrm{B})$).
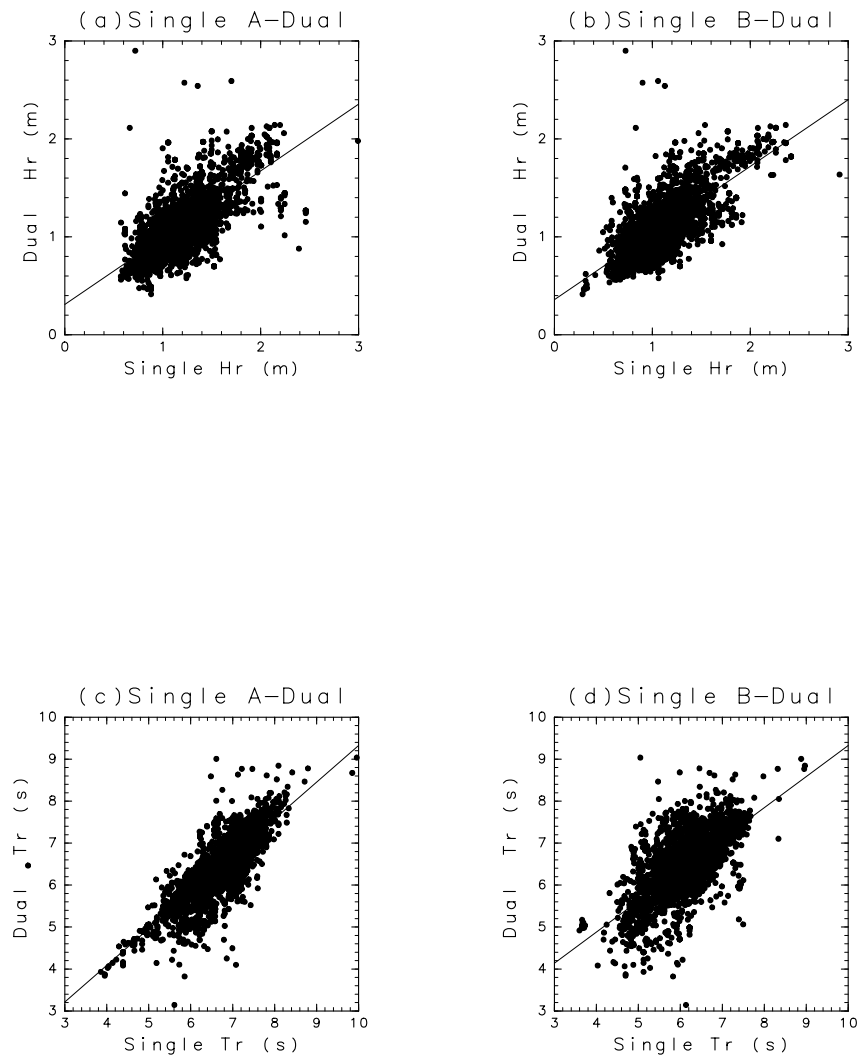
**Fig. 7** Scatter plots of wave heights. (a) Single radar A and dual radar. (b) Single radar B and dual radar. (c) As (a) but for wave periods. (d) As (b) but for wave periods.
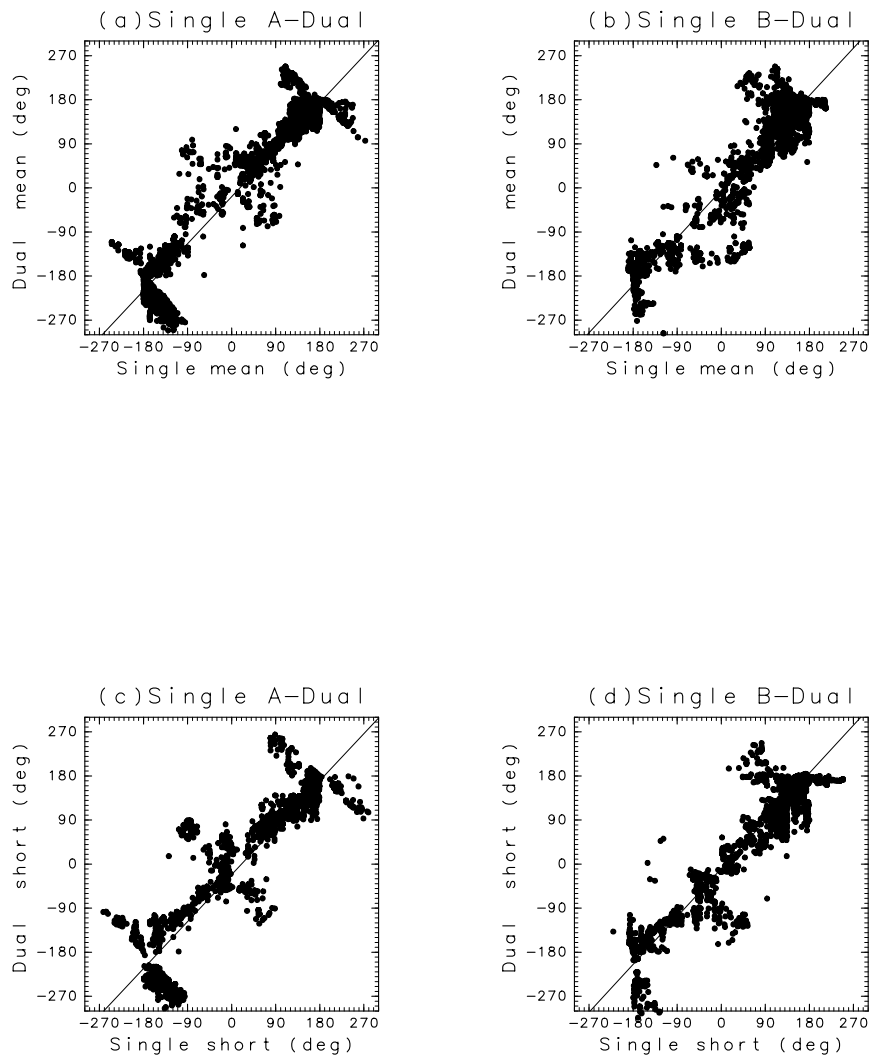
**Fig. 8** (a) As Figure 7a but for spectral mean wave directions. (b) As Figure 7b but for spectral mean wave directions. (c) As Figure 7a but for short wave directions. (d) As Figure 7b but for short-wave directions.
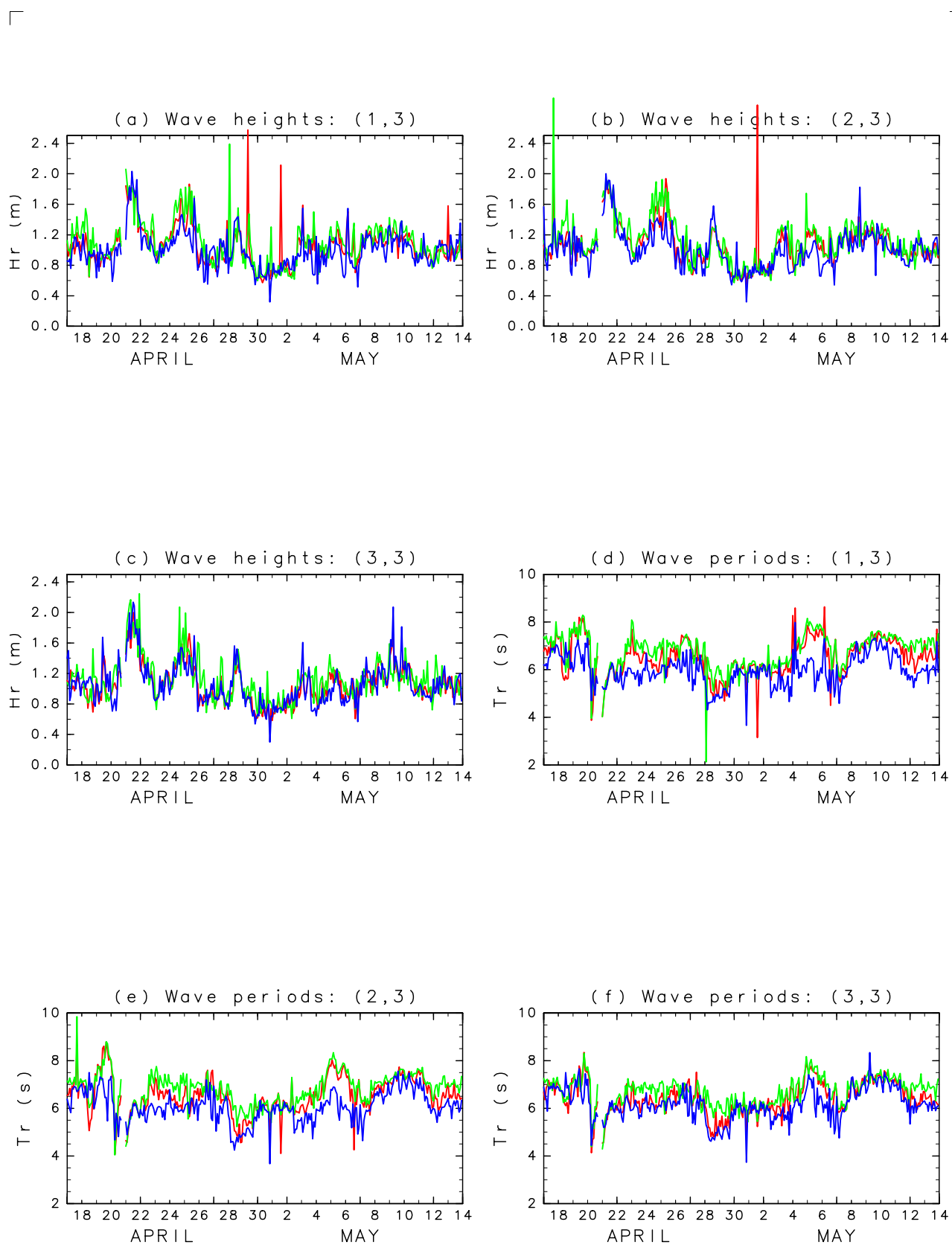
**Fig. 9** Time series of wave heights from dual radar ($H_r(\mathrm{D})$: red), single radar A ($H_r(\mathrm{A})$: green), and single radar B ($H_r(\mathrm{B})$: blue) at cell (a) $(i_x, j_y) = (1, 3)$, (b) $(i_x, j_y) = (2, 3)$, and (c) $(i_x, j_y) = (3, 3)$. (d) As (a) but for wave periods, (e) as (b) but for wave periods, and (f) as (c) but for wave periods,
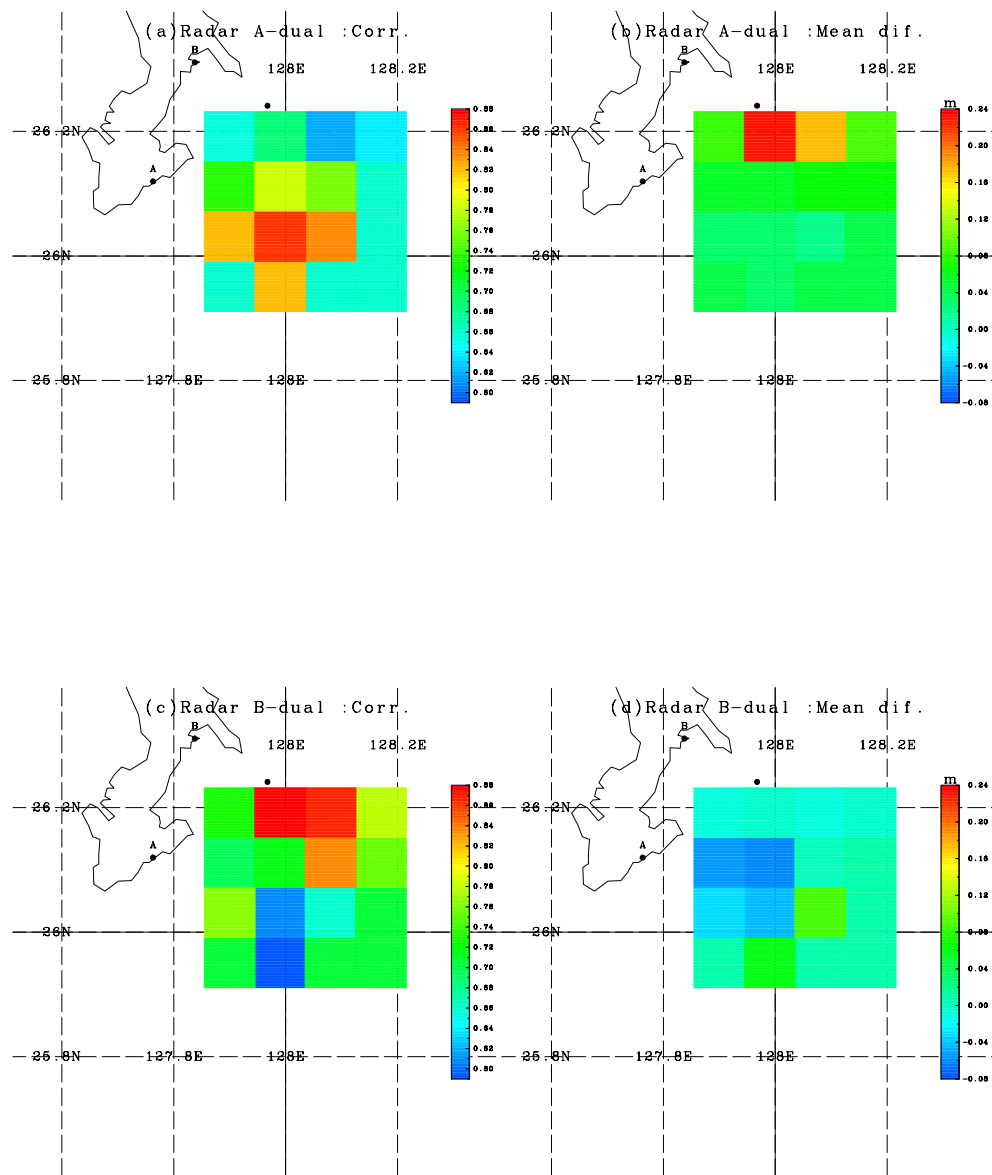
**Fig. 10** Comparisons of wave heights between those obtained from single radar and those from dual radar. (a) Correlation of dual-radar-estimated wave heights with single-radar-A-estimated wave heights. (b) As (a) but for the mean difference $(H_r(A) - H_r(A))$. (c) As (a) but for single-radar-B-estimated wave heights. (d) As (b) but for single-radar-B-estimated wave heights.
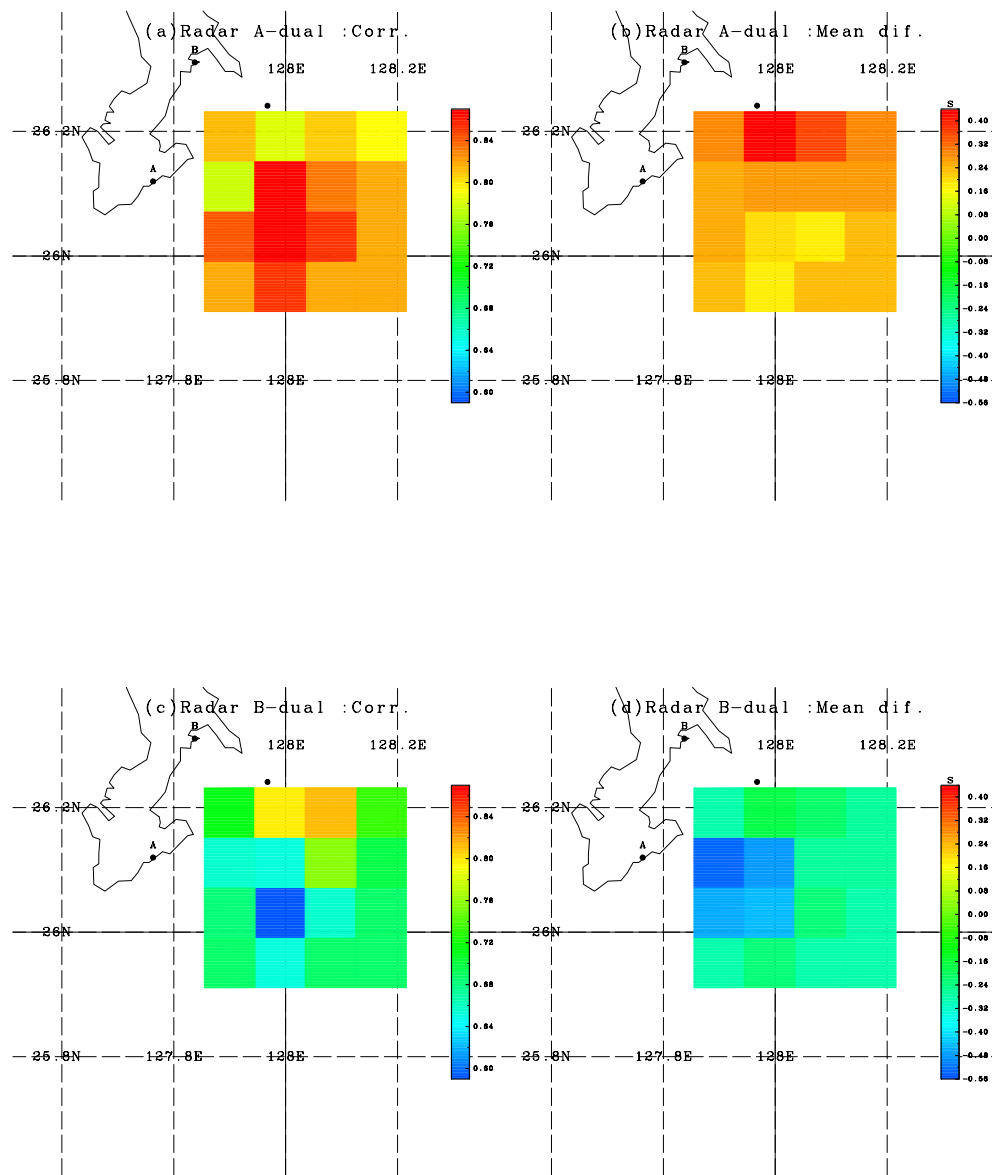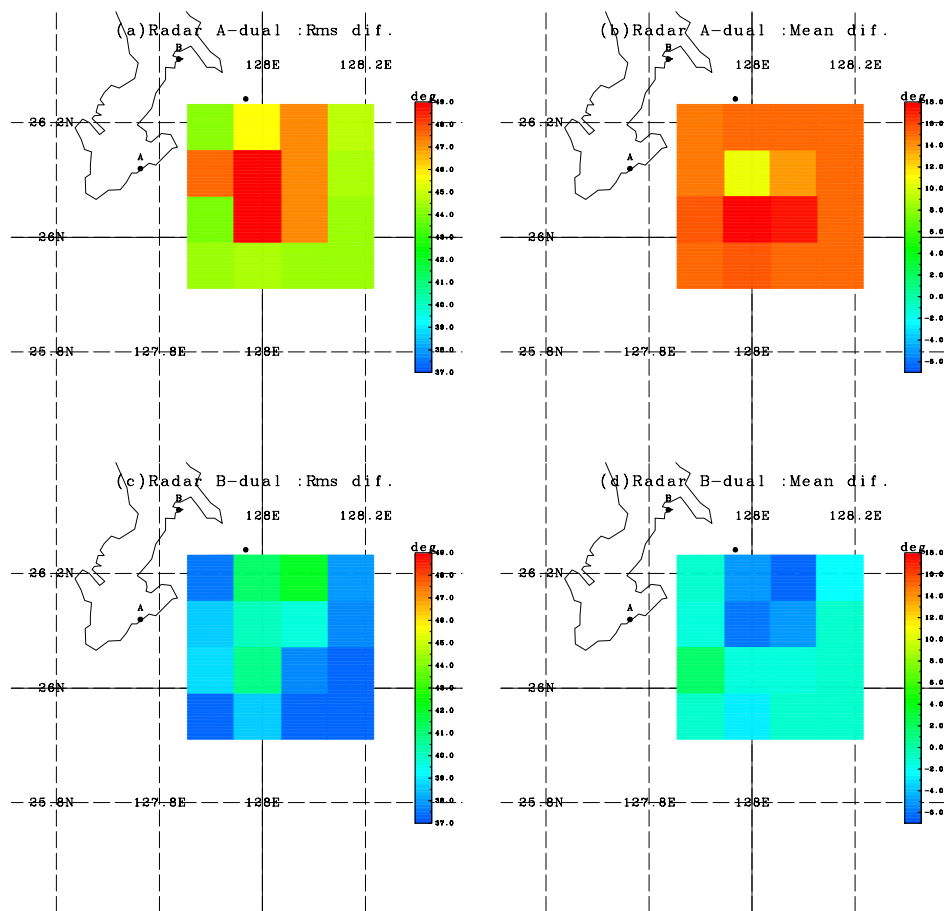
**Fig. 11** As Figure 10 but for wave period.

**Fig. 12** Comparisons of spectral mean wave directions between single radar and dual radar. (a) The rms difference between dual-radar-estimated spectral mean wave directions ($\theta_m(D)$) and single-radar A-estimated spectral mean wave directions ($\theta_m(A)$). (b) As (a) but for the mean difference ($\theta_m(A) - \theta_m(D)$). (c) As (a) but for single-radar-B-estimated spectral mean wave directions. (d) As (b) but for single-radar B-estimated ($\theta_m(B) - \theta_m(D)$) spectral mean wave directions.